

Performance augmentation mechanism of tandem flapping foils with stroke time-asymmetry

Wang, Guangjian; Ng, Bing Feng; Teo, Zhen Wei; Lua, Kim Boon; Bao, Yan

2021

Wang, G., Ng, B. F., Teo, Z. W., Lua, K. B. & Bao, Y. (2021). Performance augmentation mechanism of tandem flapping foils with stroke time-asymmetry. *Aerospace Science and Technology*, 117, 106939-. <https://dx.doi.org/10.1016/j.ast.2021.106939>

<https://hdl.handle.net/10356/154114>

<https://doi.org/10.1016/j.ast.2021.106939>

© 2021 Elsevier Masson SAS. All rights reserved. This paper was published in *Aerospace Science and Technology* and is made available with permission of Elsevier Masson SAS.

Downloaded on 13 Mar 2024 15:54:46 SGT

Performance augmentation mechanism of tandem flapping foils with stroke time-asymmetry

Guangjian Wang, Bing Feng Ng, Zhen Wei Teo, Kim Boon Lua, Yan Bao

Please cite this article as: G. Wang, B. F. Ng, Z. W. Teo, K. B. Lua, Y. Bao, “Performance augmentation of tandem flapping wings in asymmetric flapping strokes”, Aerospace Science and Technology, vol. 117, pp. 106939, 2021. DOI: <https://doi.org/10.1016/j.ast.2021.106939>

This document is the unedited author's version of a Submitted Work that was subsequently accepted for publication in Aerospace Science and Technology. To access the final edited and published work see <https://doi.org/10.1016/j.ast.2021.106939>

Publication Date: October, 2021

Performance augmentation mechanism of tandem flapping foils with stroke time-asymmetry

Guangjian Wang ^{a, b}, Bing Feng Ng ^{a, *}, Zhen Wei Teo ^a, Kim Boon Lua ^c, Yan Bao ^d

^a School of Mechanical and Aerospace Engineering, Nanyang Technological University, 50 Nanyang Avenue, Singapore, 639798

^b Singapore Centre for 3D Printing, School of Mechanical and Aerospace Engineering, Nanyang Technological University, 50 Nanyang Avenue, Singapore, 639798

^c Department of Mechanical Engineering, National Yang Ming Chiao Tung University, Hsinchu, 30010, Taiwan, ROC

^d School of Naval Architecture, Ocean and Civil Engineering, Shanghai Jiao Tong University, 800 Dongchuan Road, Minhang, Shanghai, China

Abstract

The performance augmentation mechanism of a tandem-foil system undergoing time-asymmetric flapping with unequal up- and downstroke durations (velocities) is investigated at three different phase angles, 0°, 90°, and 180°. Specifically, an asymmetry ratio, ranging from 0 to 0.4, is introduced to quantify the degree of the stroke time-asymmetry and to serve as the primary kinematic parameter of interest that affects the foil performances. Numerical simulations are implemented to predict the force production and to investigate the associated mechanism at different asymmetry ratios and phase angles. Validations are performed using digital particle image velocimetry in water tunnel experiments with two identical 3D printed wings. The results suggest that the foil performances at proper phase angles can be enhanced by stroke time-asymmetry. The force production during in-phase flapping obtains 15% increments while that during counterstroke flapping achieves remarkable enhancements by 2.5 times, as the asymmetry ratio increases from 0 to 0.4. The study also demonstrates that such enhancements are achieved through the changes in foil flapping velocities and foil-vortex interactions between the unequal up and downstrokes. These findings not only provide insights toward the characteristics of tandem foils which are operated in non-sinusoidal flapping strokes but also offer a reference to the design of efficient wing kinematics for high-performance biomimetic propulsors.

Keywords

tandem flapping foils, stroke time-asymmetry, foil-vortex interactions, digital particle image velocimetry, biomimetic

1. Introduction

The outstanding manoeuvrability of flying insects with tandem flapping wings has long served as a source of inspiration for the development of micro-aerial vehicles (MAVs) [1–3]. By mimicking insects such as dragonflies, the optimised coordination of the fore- and hindwings can enhance the propulsive performances of MAVs and introduce unique flight capabilities. Previous studies have demonstrated that the characteristics of tandem foils were affected by a range of kinematic parameters, including the flapping frequency, pitching amplitude, inter-foil spacing, and phase angle [4–7]. However, the stroke time-asymmetry, referred to as the difference between the up- and downstroke durations of a flapping cycle is less understood, despite its common occurrence in the flapping motions of flying insects for gaining locomotion.

A significant number of studies have been conducted in recent years to investigate the underlying physics of force production on tandem foils at different flapping modes. Specifically, it had been widely demonstrated that the characteristics of tandem foils were highly affected by the phase angles between the fore- and hindfoils. In forward flight, in-phase flapping could enhance the thrust and lift production via wake capture, while out-of-phase flapping could improve the power efficiency [8–15]. On the contrary, lift production was found to be attenuated in hovering flight regardless of phase relationships [16–21]. The effects of inter-foil spacing had also been investigated numerically and experimentally. Lua et al. [15] derived a mathematical model to quantify the correlations between foil spacing and phase angles on force production. Broering & Lian [10] manifested that increasing foil spacing could cause phase lags in both thrust and lift. To understand the performance augmentation mechanism, a handful of attempts had been made to study the interactions between the hindfoils and the shed vortices from the forefoils at various conditions [5,8,11,17,18,21,22]. Foil-vortex interactions occur when the hindfoils passed through and captured a portion of the vortices that shed from the forefoils. The force production on the hindfoils could be augmented if the rotational directions of the captured vortices and the leading edge vortices (LEVs) were the same. Besides, Lagopoulos et al. [23] implemented 2D numerical simulations on deflected wakes in a tandem-foil configuration, where the hindfoil not only cancelled the wake deflection and the mean side force of the forefoil but also noticeably enhanced the thrust production at a

proper phase angle. Additionally, the performances of flexible tandem wings were experimentally studied by Zheng et al. [24] using time-resolved particle image velocimetry (PIV). Their findings concluded that the bending deformations of flexible wings could alter the phase angles, thereby varying the force production.

For stroke time-asymmetry, previous studies were mainly focused on single-foil configurations. Yu & Tong [25] investigated the flow control mechanism of a time-asymmetric flapping foil, where unequal durations and angles of attack between up- and downstrokes were introduced to enhance the foil performances. Bos et al. [26] compared the force production by simple harmonic and realistic fruit-fly flapping strokes through numerical means. Their results indicated that the non-sinusoidal kinematics of fruit flies could induce smaller drag force, thus improving the propulsive performances. To further the understanding, asymmetric pitching motions and asymmetric plunging motions were separately investigated by Xiao & Liao [27], and Lu et al. [28,29] as well as Zhang & Zhou [30], who arrived at similar conclusions that proper asymmetric motions could improve foil characteristics. Zhu & Zhou [31] numerically demonstrated that asymmetric flapping strokes were beneficial to the force production in hovering flight, but not in forward flight. Moreover, Wang et al. [32] suggested that lift production could be effectively enhanced at faster downstroke flapping velocities and larger angles of attack. Liu et al. [33] visualised the unsteady flow structures generated by two foils undergoing asymmetric pitching motions in a biplane configuration using the laser-induced fluorescence method (LIF) and the finite-time Lyapunov exponents (FTLE) method. Based on their results, the stroke time-asymmetry was proved to be a critical kinematic parameter influencing wake turbulence by introducing jet-like behaviours for thrust production. More recently, Nian et al. [34] designed a compliant joint structure to study the aerodynamics of flexible flapping wings undergoing asymmetric deformations between up- and downstrokes. The results of wind tunnel experiments demonstrated that the power consumptions of the flexible wings were effectively reduced by the asymmetric flapping kinematics.

While the effects of time-asymmetric flapping on single-foil systems had been investigated by several researchers, to the best of the authors' knowledge, none of the studies considered such kinematics on tandem foils. As such, the objectives of this investigation are to seek possible enhancements to the force production on tandem foils through stroke time-asymmetry, and to elucidate the associated mechanism. An asymmetry ratio, ranging from 0 to 0.4, is introduced to describe the time-asymmetric flapping kinematics. Numerical simulations using

Computational Fluid Dynamics (CFD) are implemented to predict the instantaneous force production and flow behaviours. Experimental flow field measurements using digital particle image velocimetry (DPIV) are conducted to validate the numerical results, as this method had been extensively applied to capture the unsteady flow behaviours over flapping foils [35]. The rest of the paper is organized into three sections. Section 2.1 introduces the foil flapping kinematics. Section 2.2 and Section 2.3 describe the experimental and computational setups, respectively. Section 3 elucidates the instantaneous force production on tandem foils and the associated mechanism at different asymmetry ratios and phase angles. In Section 4, conclusions are provided.

2. Methodology

2.1 Foil Kinematics

Two identical flapping foils undergoing time-asymmetric stroke cycles in a tandem configuration are considered as shown in Figure 1(a). The foil sections are uniform along their spans and of an elliptical profile with a chord length c of 40 mm and a maximum thickness of 5 mm. The two foils are separated $2c$ apart in a uniform freestream of constant velocity at 0.125 m/s to simulate a forward flight condition with Reynolds number of 5000 as in the mid-range of insect flight [10]. The flapping frequency f is fixed at 0.67 Hz, which gives a Strouhal number of 0.32, representative of most natural fliers in the efficient cruising range of 0.2 to 0.4 [36].

The tandem foils are operated in time-asymmetric flapping strokes with unequal up- and downstroke durations at three different phase angles φ , 0° , 90° , and 180° . The flapping kinematic functions are described in terms of an asymmetry ratio δ , which is defined as the difference between the up- and downstroke durations of a flapping cycle,

$$\delta = \frac{t_u - t_d}{T} \quad (1)$$

where t_u and t_d are the up- and downstroke durations, and T is the period of a complete flapping stroke cycle, respectively. Thus, a larger value of δ indicates a shorter downstroke duration and a longer upstroke duration, that is a faster downstroke flapping velocity and a slower upstroke flapping velocity. In this study, only $\delta \geq 0$ is considered since the flapping trajectories are just flipped upside down with each other when two values of δ arrive at the same magnitude but of opposite signs, resulting in an equal magnitude of force production.

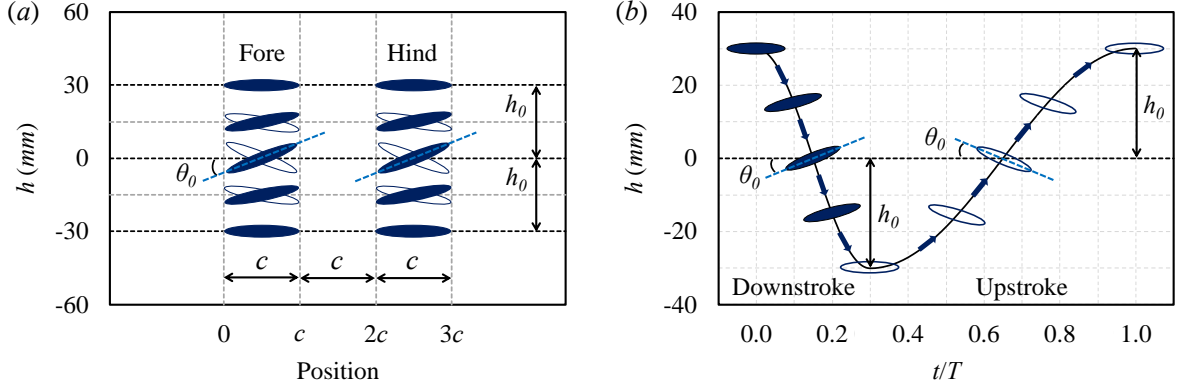


Figure 1. Schematics of the tandem foils: (a) the kinematics of the fore- and hindfoils in a tandem configuration, and the definitions of parameters; (b) the trajectory of a time-asymmetric flapping stroke cycle with unequal up- and downstroke durations (velocities) at $\delta = 0.4$.

Figure 1(b) illustrates the trajectory of a typical time-asymmetric flapping stroke cycle involved in this study, which is a combination of heaving $h(t)$ and pitching $\theta(t)$ with unequal up- and downstroke durations. Therefore, the time-asymmetric flapping kinematics can be mathematically expressed as alternate sinusoidal motions between up- and downstrokes as follow:

$$h(t) = \begin{cases} h_0 \cos\left(\frac{2\pi f}{1-\delta}t + \varphi\right), & \frac{\varphi(\delta-1)}{2\pi f} + \frac{n}{f} < t < \frac{(\varphi-\pi)(\delta-1)}{2\pi f} + \frac{n}{f} \\ h_0 \cos\left(\frac{2\pi f}{1+\delta}t - \frac{2\pi}{1+\delta} + \varphi\right), & \frac{(\varphi-\pi)(\delta-1)}{2\pi f} + \frac{n}{f} < t < \frac{\varphi(\delta-1)}{2\pi f} + \frac{n+1}{f} \end{cases} \quad (2)$$

$$\theta(t) = \begin{cases} \theta_0 \sin\left(\frac{2\pi f}{1-\delta}t + \varphi\right), & \frac{\varphi(\delta-1)}{2\pi f} + \frac{n}{f} < t < \frac{(\varphi-\pi)(\delta-1)}{2\pi f} + \frac{n}{f} \\ \theta_0 \sin\left(\frac{2\pi f}{1+\delta}t - \frac{2\pi}{1+\delta} + \varphi\right), & \frac{(\varphi-\pi)(\delta-1)}{2\pi f} + \frac{n}{f} < t < \frac{\varphi(\delta-1)}{2\pi f} + \frac{n+1}{f} \end{cases} \quad (3)$$

where the heaving amplitude h_0 is $0.75c$ and the pitching amplitude θ_0 is 30° . The dimensional time is given by t . n denotes the number of stroke cycles. To account for different phase angles, φ varies among 0° , 90° , and 180° accordingly in the hindfoil kinematic functions. Besides, a phase difference of 90° between the heaving and pitching is adopted to maximize the foil propulsive efficiency. Table. 1 summarizes the kinematic parameters of interest for the DPIV experiments and CFD numerical simulations involved in this study.

The performances of the tandem foils can be characterized by a variety of indicators, including the forefoil thrust coefficient C_{TF} , the hindfoil thrust coefficient C_{TH} , the forefoil lift coefficient

C_{LF} , the hindfoil lift coefficient C_{LF} , the forefoil pressure coefficient C_{PF} , and the hindfoil pressure coefficient C_{PH} ,

$$C_{TF} = \frac{F_{TF}}{0.5\rho U_\infty^2 c}, C_{TH} = \frac{F_{TH}}{0.5\rho U_\infty^2 c} \quad (4)$$

$$C_{LF} = \frac{F_{LF}}{0.5\rho U_\infty^2 c}, C_{LH} = \frac{F_{LH}}{0.5\rho U_\infty^2 c} \quad (5)$$

$$C_{PF} = \frac{P_F - P_\infty}{0.5\rho U_\infty^2}, C_{PH} = \frac{P_H - P_\infty}{0.5\rho U_\infty^2} \quad (6)$$

F_{TF} and F_{TH} are the thrust forces on the fore- and hindfoils in the opposite direction to the freestream. F_{LF} and F_{LH} are the lift forces on the fore- and hindfoils in the transverse direction to the freestream. P_F and P_H are the surface pressure on the fore- and hindfoils. P_∞ is the freestream pressure and ρ is the fluid density. The thrust and lift coefficients of the tandem-foil system, C_{TS} and C_{LS} , therefore can be expressed as:

$$C_{TS} = \frac{F_{TF} + F_{TH}}{0.5\rho U_\infty^2 (c_F + c_H)} = \frac{1}{2} \left(\frac{F_{TF}}{0.5\rho U_\infty^2 c} + \frac{F_{TH}}{0.5\rho U_\infty^2 c} \right) = \frac{1}{2} (C_{TF} + C_{TH}) \quad (7)$$

$$C_{LS} = \frac{F_{LF} + F_{LH}}{0.5\rho U_\infty^2 (c_F + c_H)} = \frac{1}{2} \left(\frac{F_{LF}}{0.5\rho U_\infty^2 c} + \frac{F_{LH}}{0.5\rho U_\infty^2 c} \right) = \frac{1}{2} (C_{LF} + C_{LH}) \quad (8)$$

where c_F and c_H denote the chord lengths of the fore- and hindfoils, respectively. In this study, $c_F = c_H = c$.

Table 1: Kinematic parameters of interest in this study.

Configuration	Phase Angles (φ)	DPIV Experiments	CFD Numerical Simulations
		Asymmetry Ratio δ	Asymmetry Ratio δ
Single Foil (Baseline)	--	--	0, 0.1, 0.2, 0.3, 0.4
Tandem Foils	0°, 90°, 180°	0, 0.2	0, 0.1, 0.2, 0.3, 0.4

Due to the stroke time-asymmetry, the foil locations, angles of attack and flapping velocities at the same instant are varied with δ , which poses challenges to the comparisons on results among different time-asymmetric flapping kinematics. As such, the time histories of the thrust

and lift coefficients are presented against the normalized time t^* , which is mathematically expressed as:

$$t^* = \begin{cases} \frac{ft}{1-\delta}, & 0 \leq ft \leq \frac{1-\delta}{2} \\ \frac{ft+\delta}{1+\delta}, & \frac{1-\delta}{2} \leq ft \leq 1. \end{cases} \quad (9)$$

t^* transforms different time-asymmetric flapping kinematic functions into the same simple harmonic form. At any given value of t^* , the foils undergoing different δ reach the same location with the same angle of attack, but at different magnitudes of velocities. The variations in force production by stroke time-asymmetry, therefore, are compared at the same t^* when the foils reach the same location and the same angle of attack. Further explanations on t^* can be found in the supplementary material.

2.2 Experimental Setup

The experimental setup primarily consists of three components that include a recirculating water tunnel with a test section of $450 \times 450 \times 1000$ mm, a flapping mechanism, and a digital particle image velocimetry (DPIV) system. The bottom and sides of the test section are made of tempered glass, which allows for optical measurement. The freestream velocity U_∞ was maintained at 0.125 m/s by an axial pump with a frequency inverter speed controller. Four stepper motors installed on the top of the water tunnel were used to drive the flapping motions. A pair of wings in a tandem configuration were mounted tightly to the flapping mechanism. The tandem wings were 3D printed using carbon fibre material which can provide high stiffness to minimize the bending deformations due to water flow. The hindwing was fixed $2c$ downstream of the forewing, which was of sufficient proximity to avoid delays in foil-vortex interactions. To execute the foil kinematics, Eq.2 and Eq.3 were interpreted accordingly through curve fitting to extract data points that matched with the resolution of the motors for subsequent input into the control system.

In terms of the DPIV system, a 2 W, 532 nm continuous-wave diode-pumped solid-state laser was illuminated to visualise the flow patterns on the plane of interest, which was horizontally aligned to the midspan of the tandem wings in the water tunnel. The laser beam was expanded into a 2 mm thick laser sheet [37] through optical instruments. Polyamide seeding particles with a density of 1.03 g/cm^3 and a diameter of $20 \mu\text{m}$, were added into the water to scatter the laser light. Two high-speed imaging cameras, each covering a physical view of $4c \times 4c$ with a

resolution of 1024×1024 pixels, were placed under the water tunnel in a tandem configuration to capture the flow behaviours by the flapping wings. The total physical view is $6c \times 4c$ as the two cameras had a 50% overlapped view on each other.

The images were processed with PIVlab [38]. The time interval between each frame was 10 ms. This value was checked after each run to ensure that the average particle shift was approximately less than 25% of the final interrogation window size. The multigrid approach was used, from an interrogation window size of 128×128 pixels to 64×64 pixels and finally 32×32 pixels. A 50% overlap was used for a higher vector spatial resolution. The final resulting vector map had a spatial resolution of $0.064c$. Particle displacements larger than half of the final interrogation window size were rejected and replaced by interpolation. A Gaussian 2·3-point fit algorithm was used to achieve sub-pixel precision. The uncertainty caused by a random error in the magnitude of velocity, for a particle displacement of 8 pixels was around 1.25%. The error due to scaling was less than 0.2% by using a precision ruler. As the opaque wings blocked the laser sheet, information on the velocity field was lost. Hence, each set of experiments was repeated with the reversed wing motion and the velocity fields were averaged and stitched together to minimize areas with lost information. Images for 40 flapping cycles were captured after the flow had reached a periodic state. Ensemble-averaged velocity and vorticity fields around the tandem wings at different time-asymmetric flapping modes were thereafter extracted.

2.3 Computational Setup and Validation

Unsteady incompressible Navier-Stokes equations are solved to simulate the flow regimes of the 2D tandem foils undergoing time-asymmetric flapping motions at a Reynolds number of 5000. The governing equations are described as:

$$\frac{\partial u}{\partial x} + \frac{\partial v}{\partial y} = 0 \quad (10)$$

$$\frac{\partial u}{\partial t} + u \frac{\partial u}{\partial x} + v \frac{\partial u}{\partial y} = -\frac{1}{\rho} \frac{\partial p}{\partial x} + \nu \left(\frac{\partial^2 u}{\partial x^2} + \frac{\partial^2 u}{\partial y^2} \right) \quad (11)$$

$$\frac{\partial v}{\partial t} + u \frac{\partial v}{\partial x} + v \frac{\partial v}{\partial y} = -\frac{1}{\rho} \frac{\partial p}{\partial y} + \nu \left(\frac{\partial^2 v}{\partial x^2} + \frac{\partial^2 v}{\partial y^2} \right) \quad (12)$$

where u and v are the flow velocities in x and y directions, and p is the flow pressure. The computational domain with a rectangular area of $60c \times 30c$ in Figure 2(a) is aligned to the midspan of the foils, which corresponds to the position of the DPIV in the water tunnel. The

inlet boundary with a uniform and constant freestream velocity of 0.125 m/s is prescribed at $20c$ upstream of the tandem foils, and the pressure outlet is $40c$ downstream of the tandem foils. The lateral sides of the computational domain are set as symmetric boundaries while the two elliptic foils are defined as no-slip walls.

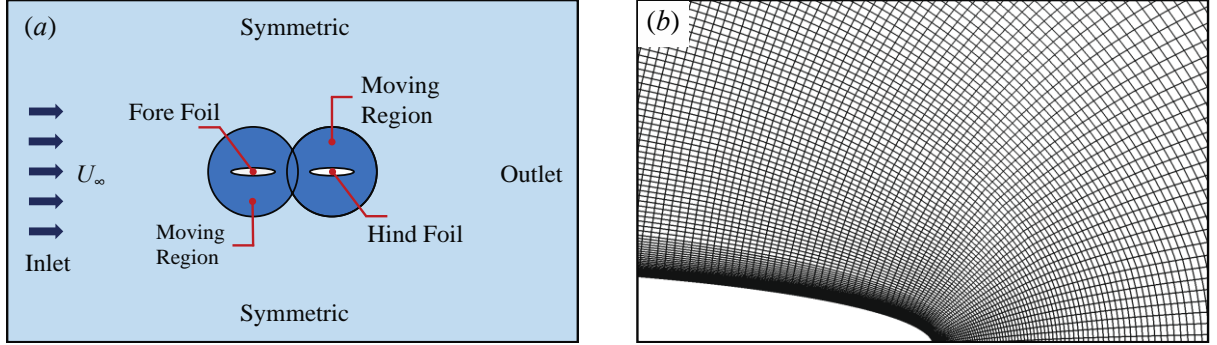


Figure 2. Computational setup: (a) the computational domain (not to scale) and the boundary conditions; (b) the boundary-conforming mesh of the flapping wings (the moving regions).

Table 2: Grid independent study.

Cases	Mesh number on foil surface	Total mesh number	\bar{C}_{TS}	Percentage difference of \bar{C}_{TS}
Mesh 1	80	132224	0.574005	--
Mesh 2	100	139432	0.570275	0.65 %
Mesh 3	200	262530	0.556875	2.35 %
Mesh 4	400	510338	0.558986	0.38 %

\bar{C}_{TS} is the mean thrust coefficient of the tandem-foil system. The percentage difference of \bar{C}_{TS} for Mesh N is calculate as $D = |\bar{C}_{TS,N} - \bar{C}_{TS,N-1}| / |\bar{C}_{TS,N}|$.

The overset mesh method is utilized to implement the heaving-to-pitching coupled motions for the tandem foils at different asymmetry ratios and phase angles, which are interpreted by Eq.2 and Eq.3, as it allows the flow domain and the near-wall regions to be separately constructed into two sets of high-quality structured meshes. The flow domain is discretized into a Cartesian mesh as a background, while the near-wall regions around the foils are constructed as

boundary-conforming meshes [39] with high resolution on the foil surfaces, as shown in Figure 2(b). The flow information is thereafter coupled between the background mesh and the near-wall mesh through interpolation points on the overlapping boundaries. A time-step size of 0.0005 s is employed for all the simulations in this study to capture the detailed dynamic patterns of the flow structures induced by the foil flapping motions.

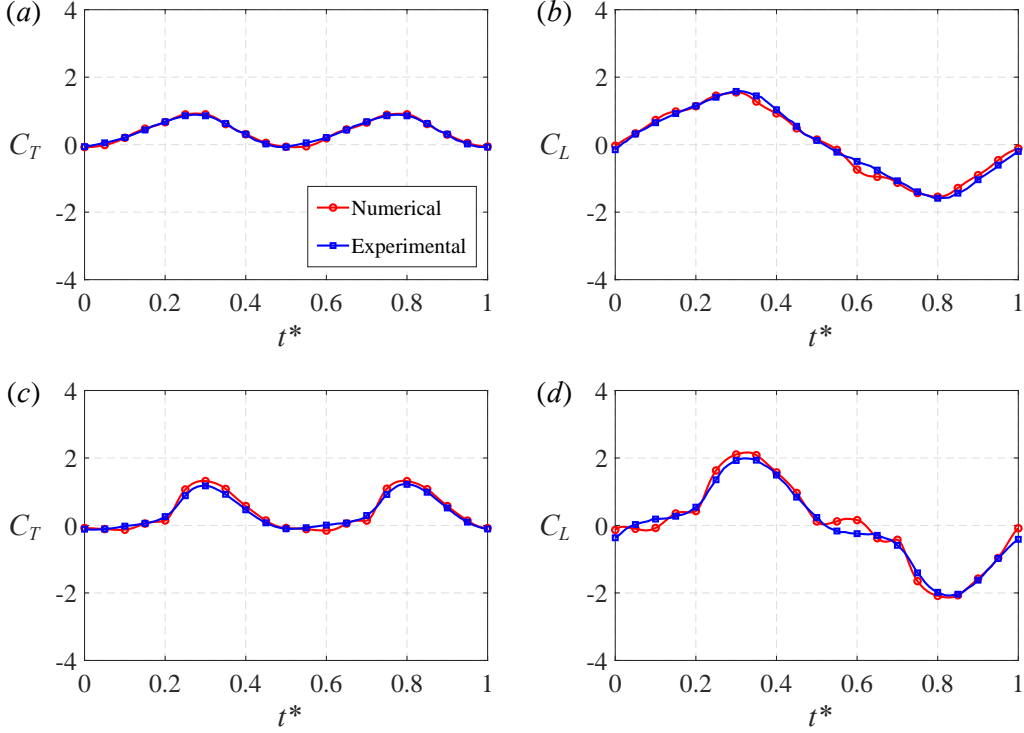


Figure 3. Validation of the CFD numerical results on instantaneous thrust and lift coefficients at $\delta = 0$ and $\varphi = 90^\circ$ against force measurement data: (a) the forefoil thrust coefficient, C_{TF} ; (b) the forefoil lift coefficient, C_{LF} ; (c) the hindfoil thrust coefficient, C_{TH} ; (d) the hindfoil lift coefficient, C_{LH} .

Based on the grid independence study in Table 2, Mesh 4 is adopted since the percentage difference of the averaged thrust coefficient between Mesh 3 and Mesh 4 is reduced to approximately 0.38%. The CFD numerical results are validated against force measurement data and DPIV experimental results. Specifically, Figure 3 indicates that the thrust and lift coefficients at $\delta = 0$ and $\varphi = 90^\circ$ predicted by CFD numerical simulation achieve a decent agreement with the force measurement data provided by Lua et al [15]. Figure 4 compares the numerical and DPIV experimental results on vorticity fields at different phase angles, where the numerical results show similar patterns as those obtained by DPIV experiments. A complete validation of the CFD numerical results is presented in the supplementary material.

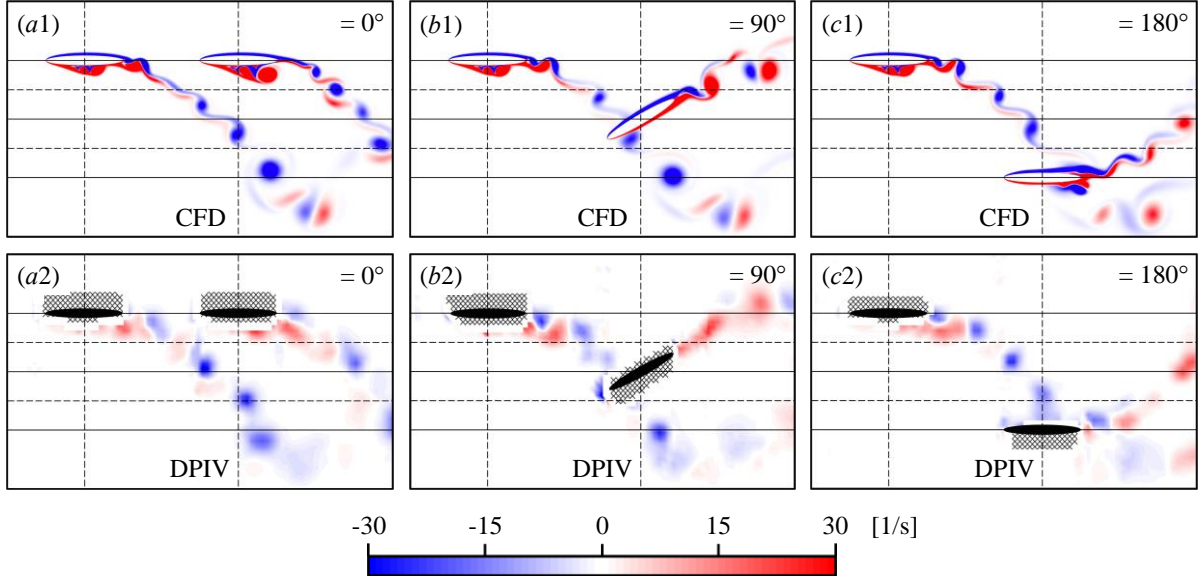


Figure 4. Validation of the CFD numerical results on vorticity fields at $\delta = 0$ against DPIV experimental data: (a1) the numerical result at $\varphi = 0^\circ$; (a2) the DPIV experimental result at $\varphi = 0^\circ$; (b1) the numerical result at $\varphi = 90^\circ$; (b2) the DPIV experimental result at $\varphi = 90^\circ$; (c1) the numerical result at $\varphi = 180^\circ$; (c2) the DPIV experimental result at $\varphi = 180^\circ$.

3. Results

3.1 Single-foil flapping

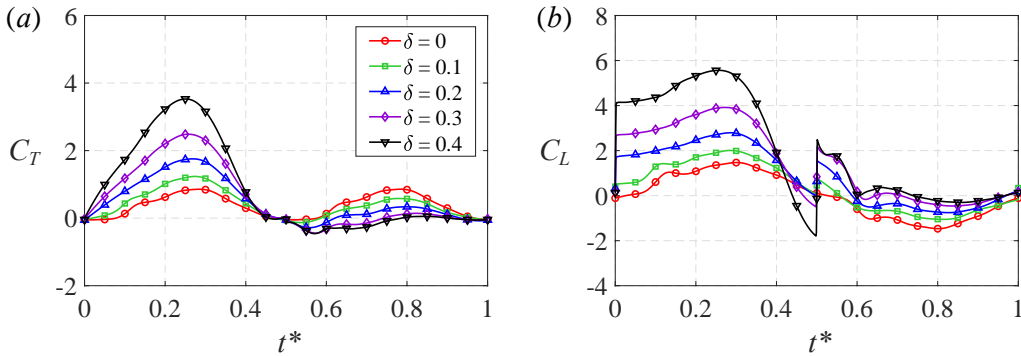


Figure 5. Instantaneous thrust and lift coefficients of the single foil at various δ : (a) the thrust coefficient; (b) the lift coefficient.

The instantaneous thrust and lift coefficients of a single foil at various δ are shown in Figure 5. It is illustrated that the thrust coefficient increases with δ during the downstroke ($t^* < 0.5$) but decreases during the upstroke ($t^* > 0.5$). The lift coefficient generally increases with δ throughout the flapping cycle. Such variations are primarily caused by the change in foil flapping velocity between the up- and downstrokes due to the stroke time-asymmetry. The magnitude of flapping velocity increases with δ during the downstroke, which results in much

stronger LEVs on the foil upper surface, as shown in Figure 6(a1), (b1) and (c1). Therefore, the pressure on the foil upper surface in Figure 7(a) becomes lower at larger values of δ , which augments the thrust and lift production. Meanwhile, the increased downstroke flapping velocity can also reinforce the pressure and shear stress on the foil lower surface, further contributing to the force production.

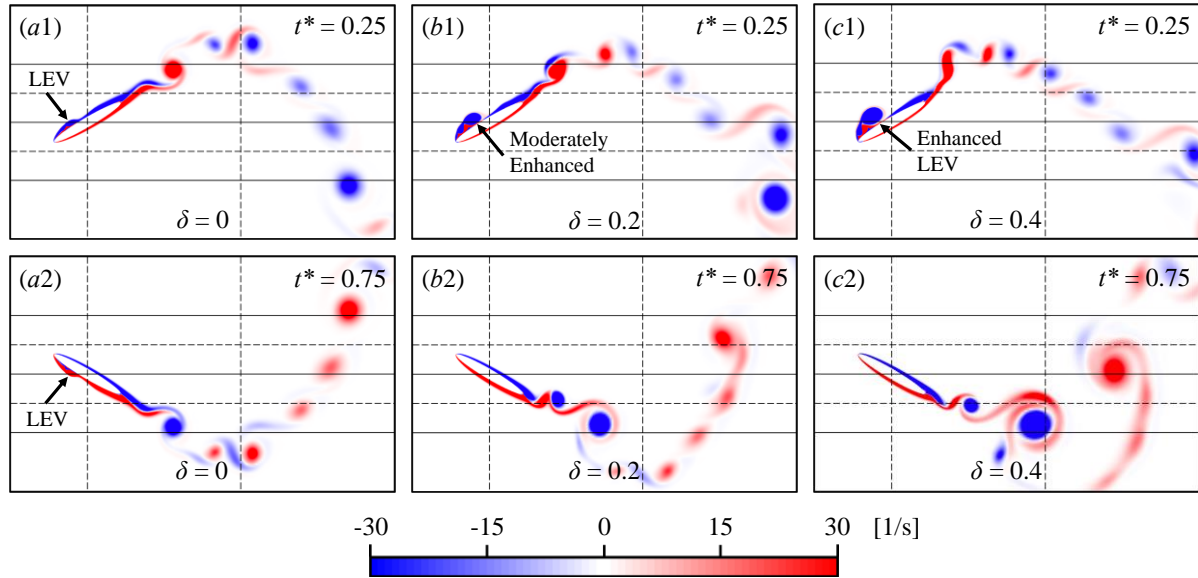


Figure 6. Instantaneous vorticity fields of the single foil at various δ : (a1) $t^* = 0.25$, $\delta = 0$; (a2) $t^* = 0.75$, $\delta = 0$; (b1) $t^* = 0.25$, $\delta = 0.2$; (b2) $t^* = 0.75$, $\delta = 0.2$; (c1) $t^* = 0.25$, $\delta = 0.4$; (c2) $t^* = 0.75$, $\delta = 0.4$.

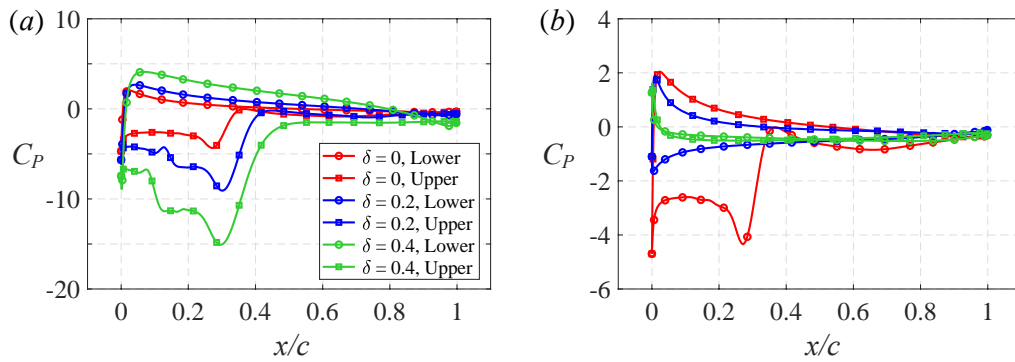


Figure 7. Instantaneous pressure coefficients of the single foil at various δ : (a) $t^* = 0.15$; (b) $t^* = 0.75$.

In contrast, the foil flapping velocity reduces with the increase in δ during the upstroke, which attenuates the formation of LEVs on the foil lower surface, as shown in Figure 6(a2), (b2) and (c2). Such reduced LEVs result in higher pressure on the foil lower surface compared to the

symmetric flapping condition as depicted in Figure 7(b). Thus, the force production is adversely affected. At $\delta > 0.2$, the thrust coefficient drops to below zero while the lift coefficient increases to above zero, probably because the force production becomes smaller than the freestream-induced drag, due to the reduction in flapping velocity. This suggests the mechanism of force production at the low flapping velocity turns to freestream-dominant.

3.2 In-phase flapping ($\varphi = 0^\circ$)

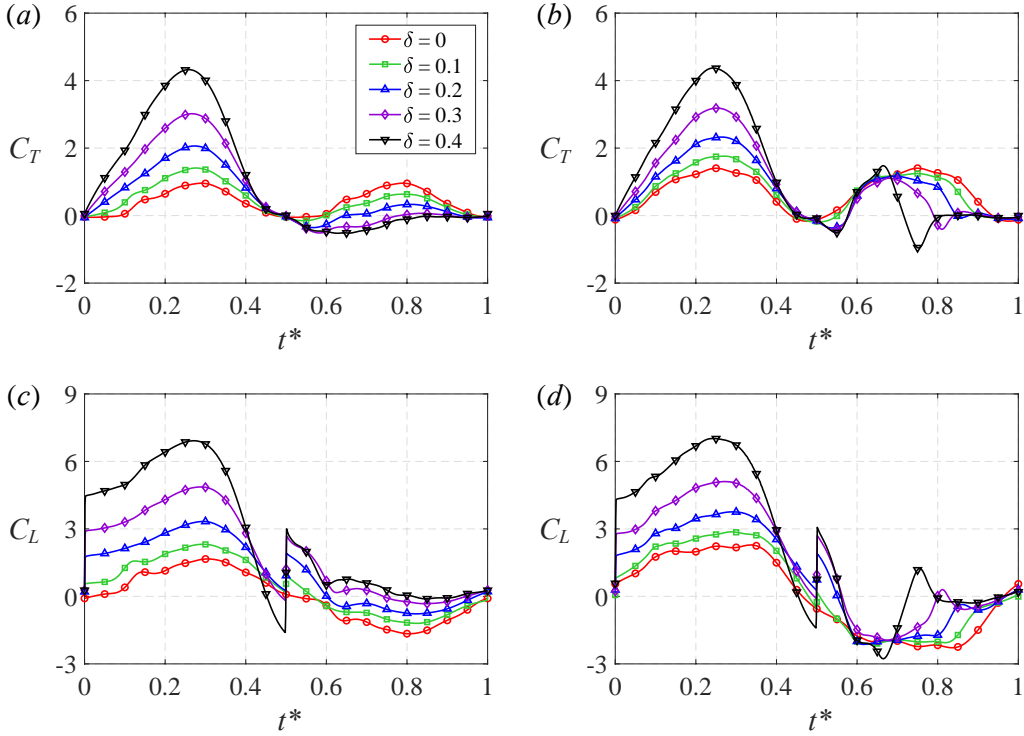


Figure 8. Instantaneous thrust and lift coefficients of the tandem foils undergoing in-phase flapping ($\varphi = 0^\circ$) at various δ : (a) the forefoil thrust coefficient, C_{TF} ; (b) the hindfoil thrust coefficient, C_{TH} ; (c) the forefoil lift coefficient, C_{LF} ; (d) the hindfoil lift coefficient, C_{LH} .

Figure 8 depicts the instantaneous thrust and lift coefficients of the tandem foils undergoing in-phase flapping against t^* at various δ . Compared with Figure 5, the force production on the forefoil is much similar to that of the single foil while the hindfoil during the upstroke illustrates a much more complicated pattern. This indicates that the effect of stroke time-asymmetry on the forefoil is mainly through the variation in flapping velocity, but the performance of the hindfoil should be also affected by other factors, like the foil-vortex interactions.

3.2.1 Downstroke of in-phase flapping

During the downstroke, the thrust and lift coefficients of both foils increase notably as δ grows from 0 to 0.4, primarily due to the increased downstroke flapping velocities. Figure 9 demonstrates that the LEVs on the foil upper surfaces are strengthened with the increase in δ , which enhances the suction effects that account for thrust and lift production on both foils. However, at the deceleration phase of the downstroke ($0.25 < t^* < 0.5$), the thrust and lift coefficients of both foils reduce more rapidly at larger values of δ . This is caused as the flapping velocities reduce rapidly at this instant. Moreover, Figure 10 illustrates that notable vortex detachments occur on the foil upper surfaces and become more significant at larger values of δ . Subsequently, the suction effects on the foil upper surfaces continuously weakened with the increase in δ , which reduces the thrust and lift production. This corresponds to the significant pressure increases at the front portions of the foil upper surfaces as shown in Figure 11. When $\delta = 0.4$, the lift coefficients drop to around -2, indicating negative lift on both foils. Such significant downforces are possibly induced by the vortex detachments and the upward motions of the leading edges against the incoming freestream at this instant.

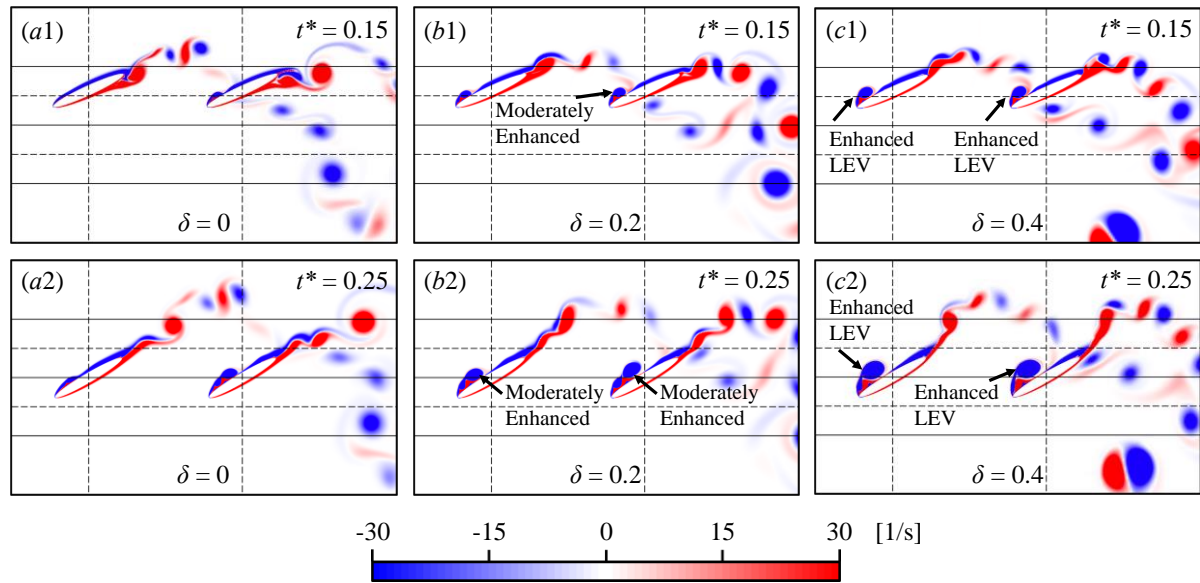


Figure 9. Instantaneous vorticity fields of the tandem foils undergoing in-phase flapping at various δ during a downstroke: (a1) $t^* = 0.15$, $\delta = 0$; (a2) $t^* = 0.25$, $\delta = 0$; (b1) $t^* = 0.15$, $\delta = 0.2$; (b2) $t^* = 0.25$, $\delta = 0.2$; (c1) $t^* = 0.15$, $\delta = 0.4$; (c2) $t^* = 0.25$, $\delta = 0.4$.

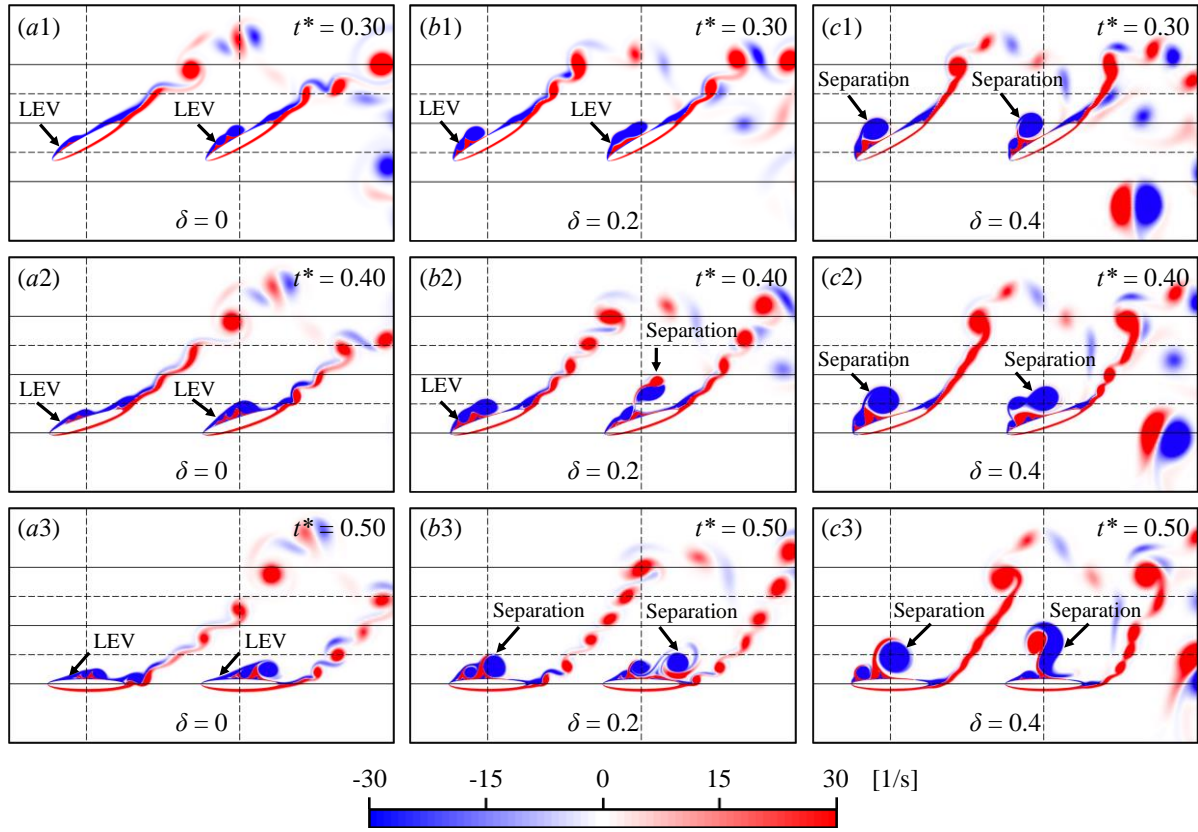


Figure 10. Instantaneous vorticity fields of the tandem foils undergoing in-phase flapping at various δ during the deceleration phase of a downstroke: (a1) $t^* = 0.3$, $\delta = 0$; (a2) $t^* = 0.4$, $\delta = 0$; (a3) $t^* = 0.5^-$, $\delta = 0$; (b1) $t^* = 0.3$, $\delta = 0.2$; (b2) $t^* = 0.4$, $\delta = 0.2$; (b3) $t^* = 0.5^-$, $\delta = 0.2$; (c1) $t^* = 0.3$, $\delta = 0.4$; (c2) $t^* = 0.4$, $\delta = 0.4$; (c3) $t^* = 0.5^-$, $\delta = 0.4$.

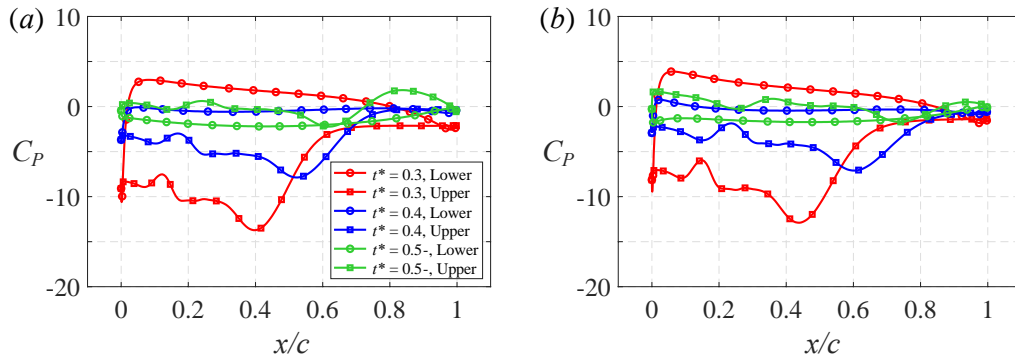


Figure 11. Instantaneous pressure coefficients of the tandem foils undergoing in-phase flapping at various δ during the deceleration phase of a downstroke: (a) the forefoil pressure coefficient, C_{PF} ; (b) the hindfoil pressure coefficient, C_{PH} . $t^* = 0.5^-$ refers to the instant just before the stroke reversal.

3.2.2 Stroke reversal of in-phase flapping

During the stroke reversal around $t^* = 0.5$, Figure 8(a) and Figure 8(b) indicate that the thrust production is adversely affected by the asymmetric flapping, as the thrust coefficients of both foils drop to below zero and become even smaller with the increase in δ . In contrast, the lift coefficients, which experience sudden surges at $t^* = 0.5$, are effectively enhanced with the increase in δ as shown in Figure 8(c) and Figure 8(d). The thrust losses and lift enhancements on both foils are associated with the reductions in flapping velocities during the stroke reversal. For larger values of δ , e. g. 0.3 and 0.4, the mechanism of force production is freestream-dominant as the foils flap up much slower with positive angles of attack, inducing significant drag and positive lift. Figure 12 describes the pressure variations between the foil upper and lower surfaces at $\delta = 0.4$ during the stroke reversal, where high-pressure regions shift rapidly from the foil upper surfaces to the lower surfaces within this time interval. Additionally, Figure 13 shows stronger vortices remaining on the foil upper surfaces at larger values of δ . Such vortices, which are generated during the previous downstroke, can be referred to as residual leading edge vortices (RLEVs) [40]. Hence, the thrust production is further hindered. For smaller values of δ , e. g. 0.1 and 0.2, the foil performances are freestream-dominant at the beginning of the upstroke. As the heaving velocities get faster with time, it gradually becomes flapping-dominant, which allows to generate thrust and negative lift.

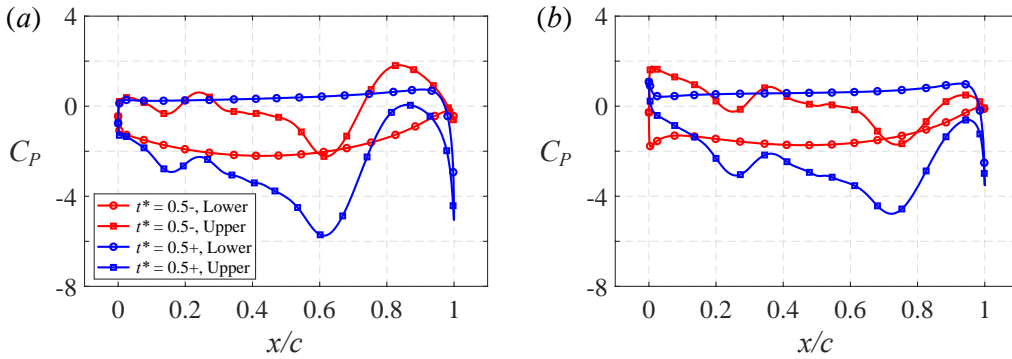


Figure 12. Instantaneous pressure coefficients of the tandem foils undergoing in-phase flapping at $\delta = 0.4$ during the stroke reversal ($t^* = 0.5^-$ and 0.5^+): (a) the forefoil pressure coefficient, C_{PF} ; (b) the hindfoil pressure coefficient, C_{PH} . $t^* = 0.5^-$ and 0.5^+ refer to the instants just before and after the stroke reversal, respectively.

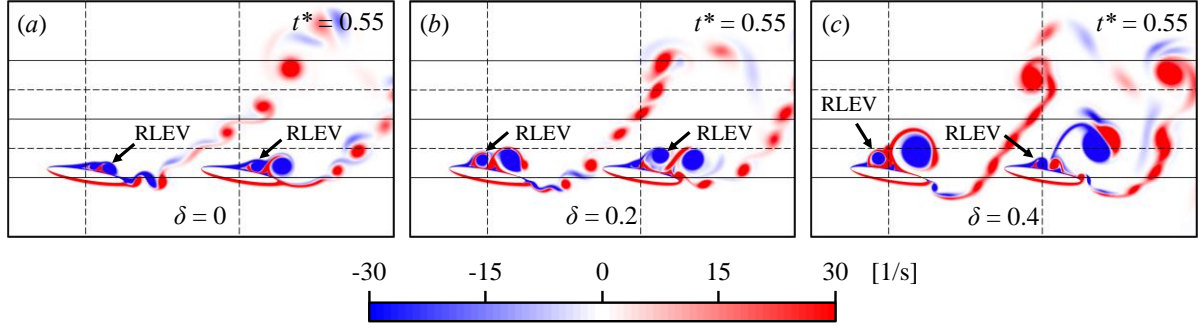


Figure 13. Instantaneous vorticity fields of the tandem foils undergoing in-phase flapping at various δ for $t^* = 0.55$: (a) $\delta = 0$; (b) $\delta = 0.2$; (c) $\delta = 0.4$.

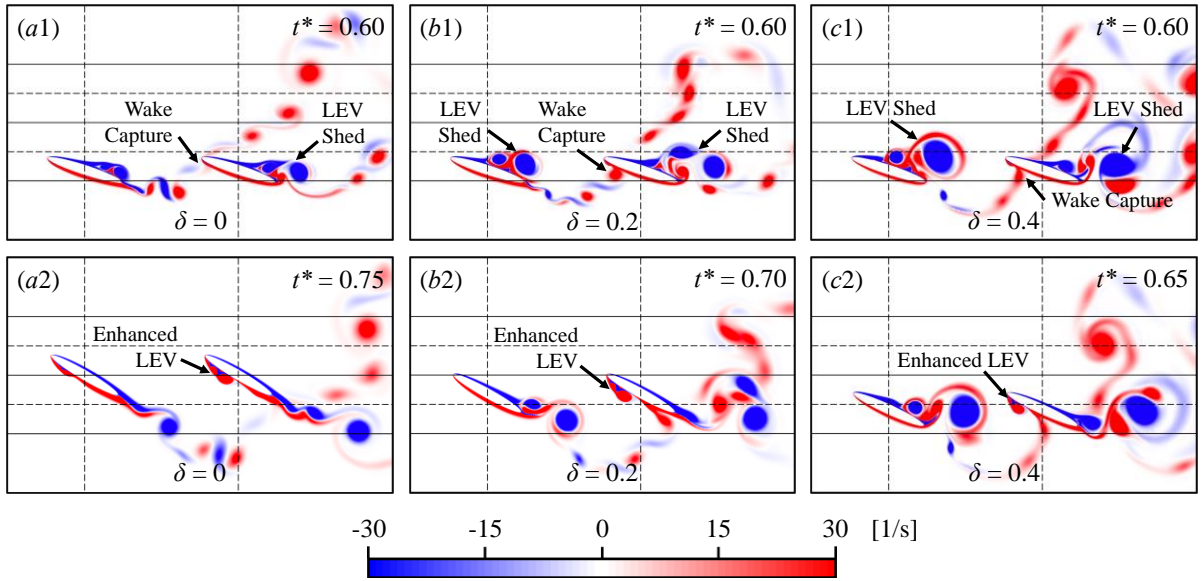


Figure 14. Instantaneous vorticity fields of the tandem foils undergoing in-phase flapping at various δ during an upstroke: (a1) $t^* = 0.6$, $\delta = 0$; (a2) $t^* = 0.75$, $\delta = 0$; (b1) $t^* = 0.6$, $\delta = 0.2$; (b2) $t^* = 0.7$, $\delta = 0.2$; (c1) $t^* = 0.6$, $\delta = 0.4$; (c2) $t^* = 0.65$, $\delta = 0.4$.

3.2.3 Upstroke of in-phase flapping

During the upstroke, Figure 8(a) and Figure 8(c) indicate that the thrust production on the forefoil is attenuated, while the lift is reinforced with the increase in δ , much similar to the single foil condition. In contrast, the thrust and lift coefficients of the hindfoil during the upstroke demonstrate more complex temporal distributions because of the foil-vortex interactions. Specifically, it can be inferred from Figure 8(a) and Figure 8(b) that the thrust production on the hindfoil during the upstroke is much larger than that on the forefoil. Figure 14 illustrates that the shed vortices via the previous downstroke of the forefoil are cut and captured by the hindfoil from $t^* = 0.6$, thus strengthening the LEVs on the lower surface of the hindfoil. Such foil-vortex interaction consequently results in high-thrust but negative lift as

indicated in Figure 8. Besides, it can also be indicated that increasing δ will lead to an earlier peaking of the upstroke thrust as the vortices shed from the forefoil via the previous downstroke are faster and more consistent.

From $t^* = 0.7$, Figure 8(b) and Figure 8(d) illustrate that during the upstroke the thrust coefficient of the hindfoil experiences an earlier downturn while the lift coefficient is subjected to an earlier upturn with the increase in δ . Technically, with the increase in δ , the thrust production on the hindfoil is reduced, but the lift production is augmented. This is likely caused by the pressure increase on the foil lower surface, as two opposite vortices form into dipole with induced velocities on each other, expediting the LEVs on the hindfoil to shed as described in Figure 15.

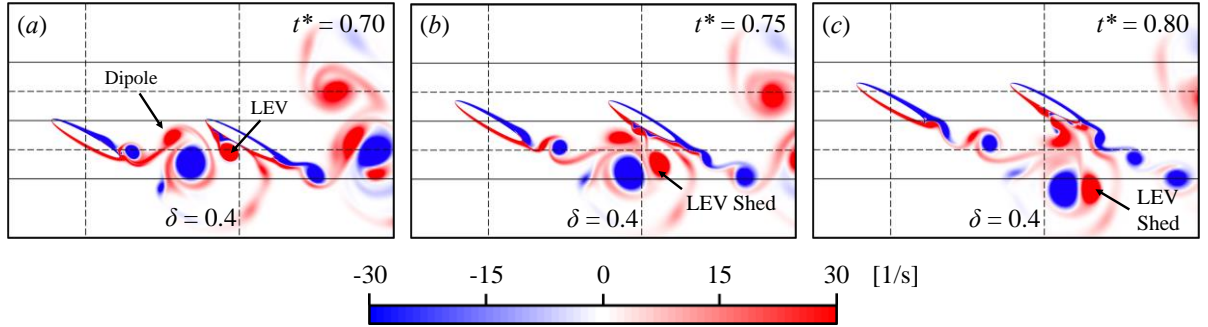


Figure 15. Instantaneous vorticity fields of the tandem foils undergoing in-phase flapping at $\delta = 0.4$: (a) $t^* = 0.7$; (b) $t^* = 0.75$; (c) $t^* = 0.8$.

3.2.4 Summary of in-phase flapping

To conclude, the thrust production on the forefoil is effectively enhanced during the downstroke but attenuated during the upstroke with the increase in δ as indicated in Figure 16(a). This suggests that the thrust production is positively related to flapping velocities. Moreover, the lift production is largely augmented throughout the whole stroke cycle as δ increases from 0 to 0.4. In terms of the hindfoil, its performances are not only affected by the variation in flapping velocities, but also the foil-vortex interactions. During the downstroke, the primary factor that augments the thrust and lift production on the hindfoil is the foil flapping velocity. The shed vortices that developed during the previous upstroke are insignificant to the force production. During the upstroke, the thrust and lift are dominant by both the flapping velocities and the foil-vortex interactions. Although the mean thrust coefficient during the upstroke reduces with the increase in δ , Figure 16(b) suggests that the existence of the foil-

vortex interaction enables it to still maintain above 0, which is a significant improvement compared with the forefoil.

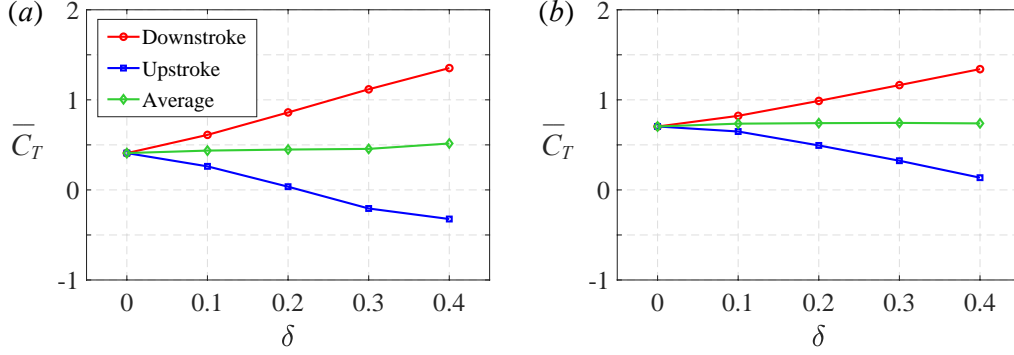


Figure 16. Mean thrust coefficients of the tandem foils at the up- and downstrokes, respectively: (a) the mean forefoil thrust coefficient; (b) the mean hindfoil thrust coefficient.

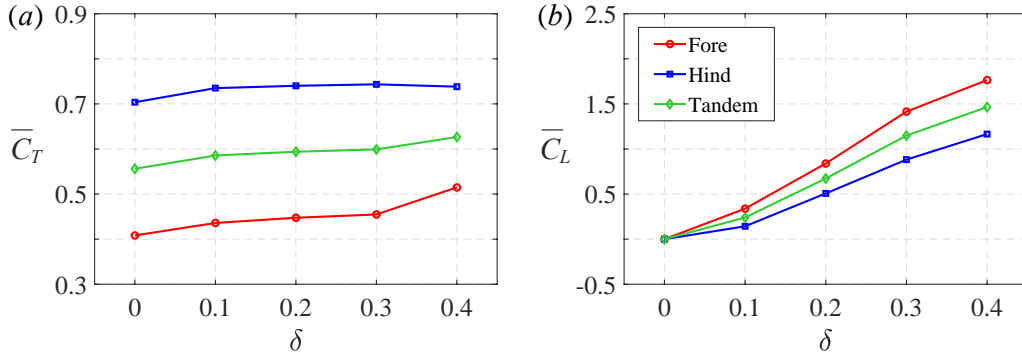


Figure 17. Mean thrust and lift coefficients of the tandem foils: (a) the mean thrust coefficients of the forefoil \bar{C}_{TF} , the hindfoil \bar{C}_{TH} , and the tandem-foil system \bar{C}_{TS} ; (b) the mean lift coefficients of the forefoil \bar{C}_{LF} , the hindfoil \bar{C}_{LH} , and the tandem-foil system \bar{C}_{LS} .

Figure 17 summarizes the mean thrust and lift coefficients of the tandem-foil system against δ . The forefoil gains a notable thrust improvement of about 25% as δ increases from 0 to 0.4, while the hindfoil demonstrates a much larger magnitude of thrust production via wake capture in Figure 17(a). It should be noted that the mean thrust coefficient of the hindfoil is only modestly enhanced with δ and reaches a plateau when $\delta > 0.1$ as the additional thrust that is obtained from the increased downstroke flapping velocity and the constructive wake capture is compensated by the reduced upstroke flapping velocity and the destructive LEV shedding. Averaging across the fore- and hindfoils, the mean thrust coefficient of the tandem-foil system \bar{C}_{TS} increases by around 15% from 0.55 to 0.63 when δ increases from 0 to 0.4. Figure 17(b)

suggests the mean lift coefficient \bar{C}_{LS} increases from 0 to 1.5 at $\delta = 0.4$, given that the faster downstroke velocities of the two foils augment the positive lift and the slower upstroke velocities generate smaller negative lift.

3.3 Counterstroke flapping ($\varphi = 180^\circ$)

The instantaneous force production on the forefoil undergoing counterstroke flapping in Figure 18(a) and Figure 18(c) demonstrate a similar pattern to that of the single foil condition. Specifically, the downstroke thrust peak is effectively enhanced while the upstroke thrust peak is attenuated with negative values at the beginning of the upstroke, as δ increases from 0 to 0.4. The lift production is enhanced throughout the whole flapping cycle. These are due to the change in flapping velocities between the up- and downstrokes as explained in Section 3.1.

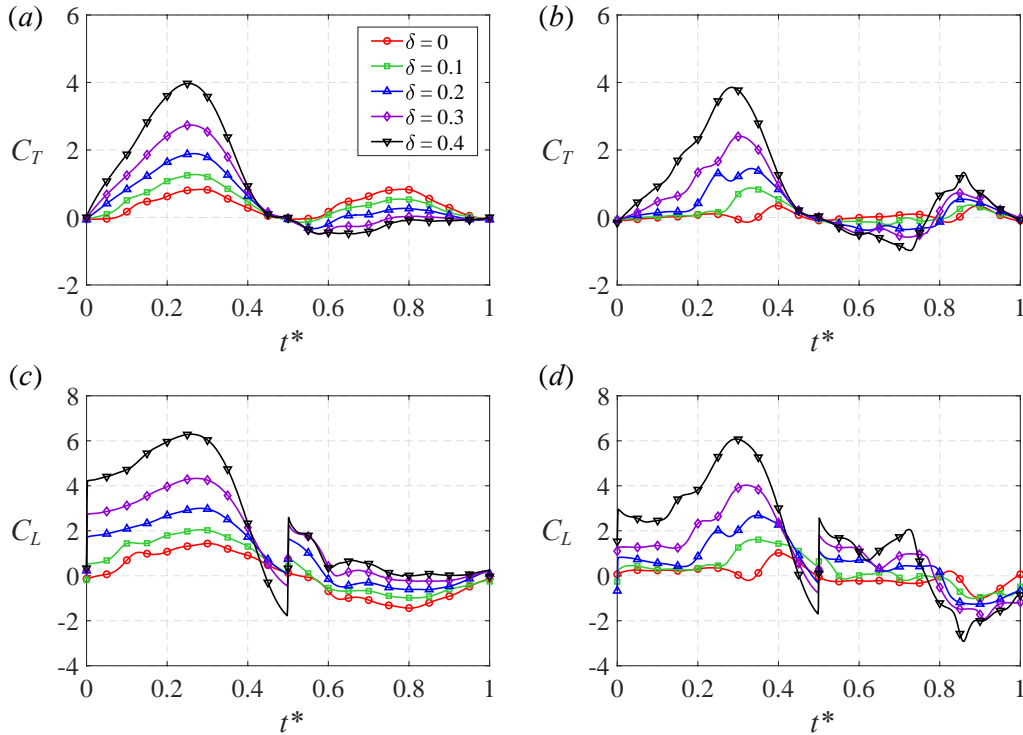


Figure 18. Instantaneous thrust and lift coefficients of the tandem foils undergoing counterstroke flapping ($\varphi = 180^\circ$) at various δ : (a) the forefoil thrust coefficient, C_{TF} ; (b) the hindfoil thrust coefficient, C_{TH} ; (c) the forefoil lift coefficient, C_{LF} ; (d) the hindfoil lift coefficient, C_{LH} .

3.3.1 Downstroke of counterstroke flapping

In terms of the hindfoil during the downstroke, Figure 18(b) and Figure 18(d) indicate that the thrust and lift coefficients increase with δ because the increased downstroke flapping velocity

can strengthen the LEV formation on the foil upper surface as shown in Figure 19. At the end of the downstroke, the lift production is again reduced with the increase in δ , as shown in Figure 18(d). Figure 20(a) suggests that the lift reduction is associated with the rapid pressure increase on the foil upper surface due to vortex detachments.

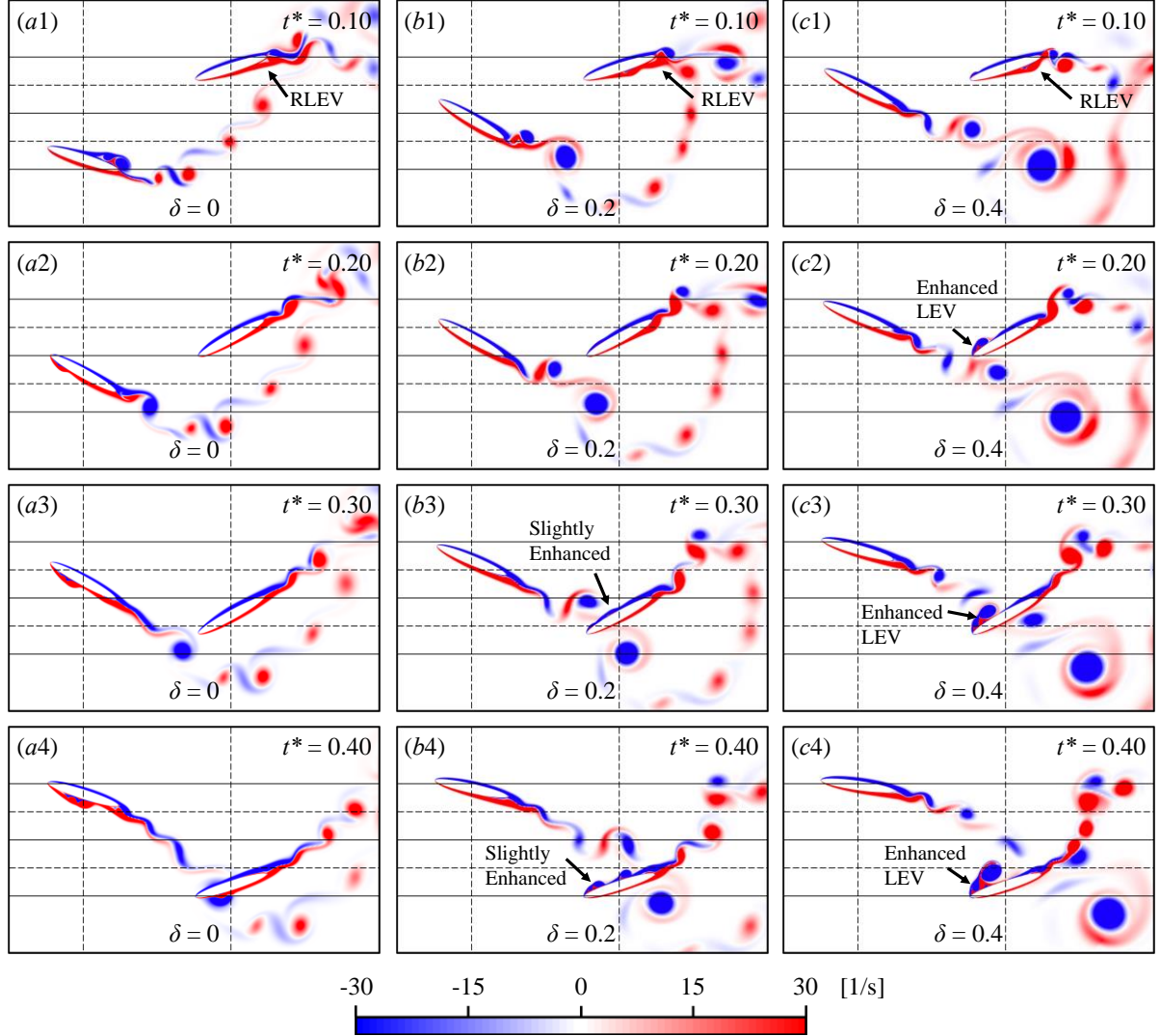


Figure 19. Instantaneous vorticity fields of the tandem foils undergoing counterstroke flapping at various δ during a hindfoil downstroke: (a1) $t^* = 0.1$, $\delta = 0$; (a2) $t^* = 0.2$, $\delta = 0$; (a3) $t^* = 0.3$, $\delta = 0$; (a4) $t^* = 0.4$, $\delta = 0$; (b1) $t^* = 0.1$, $\delta = 0.2$; (b2) $t^* = 0.2$, $\delta = 0.2$; (b3) $t^* = 0.3$, $\delta = 0.2$; (b4) $t^* = 0.4$, $\delta = 0.2$; (c1) $t^* = 0.1$, $\delta = 0.4$; (c2) $t^* = 0.2$, $\delta = 0.4$; (c3) $t^* = 0.3$, $\delta = 0.4$; (c4) $t^* = 0.4$, $\delta = 0.4$.

3.3.2 Stroke reversal of counterstroke flapping

During the stroke reversal, the force production on the hindfoil demonstrates a similar pattern to that of the in-phase flapping, where the thrust coefficient decreases to below zero but the lift

coefficient experiences a sudden surge due to the pressure enhancement on the foil lower surface as shown in Figure 20(b). The force production is freestream-dominant as the foil flaps up much slower with a positive angle of attack especially at larger values of δ , thus generating drag and positive lift. Additionally, the RLEVs on the foil upper surface in Figure 21 can also hinder the thrust production.

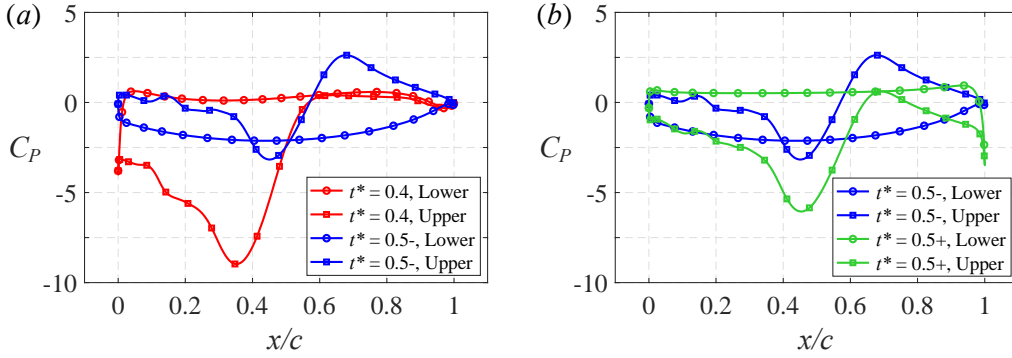


Figure 20. Instantaneous hindfoil pressure coefficients C_{PH} during counterstroke flapping at $\delta = 0.4$: (a) before the stroke reversal, $0.4 \leq t^* \leq 0.5^-$; (b) during the stroke reversal, $0.5^- \leq t^* \leq 0.5^+$.

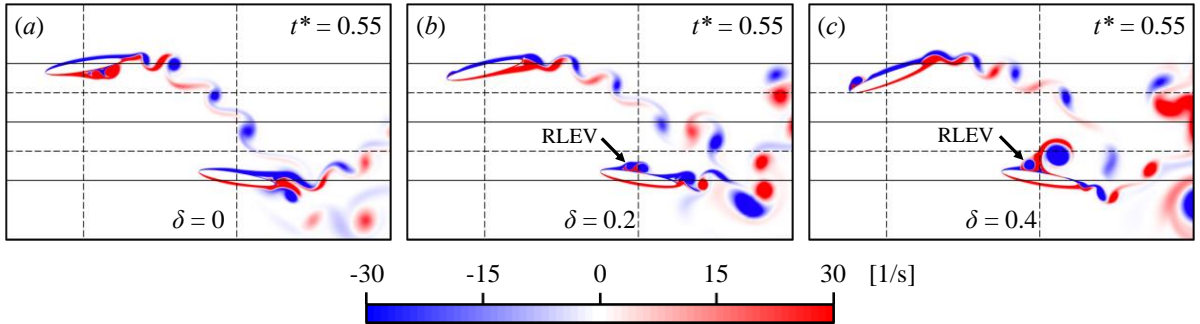


Figure 21. Instantaneous vorticity fields of the tandem foils undergoing counterstroke flapping at various δ for $t^* = 0.55$: (a) $\delta = 0$; (b) $\delta = 0.2$; (c) $\delta = 0.4$.

3.3.3 Upstroke of counterstroke flapping

During the first half of the upstroke from $t^* = 0.5$ to 0.75 , Figure 18(b) and Figure 18(d) demonstrate that the thrust coefficient of the hindfoil maintains at a very low level and generally decreases with time to below zero, but the lift coefficient experiences an increase. At larger values of δ , the thrust coefficient reduces to even smaller while the lift ascends to higher. The mechanism of force production becomes freestream-dominant within this time interval. At larger values of δ , the hindfoil flaps up much slower, thus resulting in stronger drag and positive

lift. Moreover, the hindfoil continuously approaches the forefoil as illustrated in Figure 22. Therefore, the drag forces are further reinforced by the induced flow velocities behind the forefoil. Such effect augments with the increase in δ due to the increased downstroke velocity of the forefoil. In addition, the RLEVs on the hindfoil in Figure 23 become stronger as δ increases, which also adversely affects the thrust production but enhances the positive lift for high asymmetric flapping.

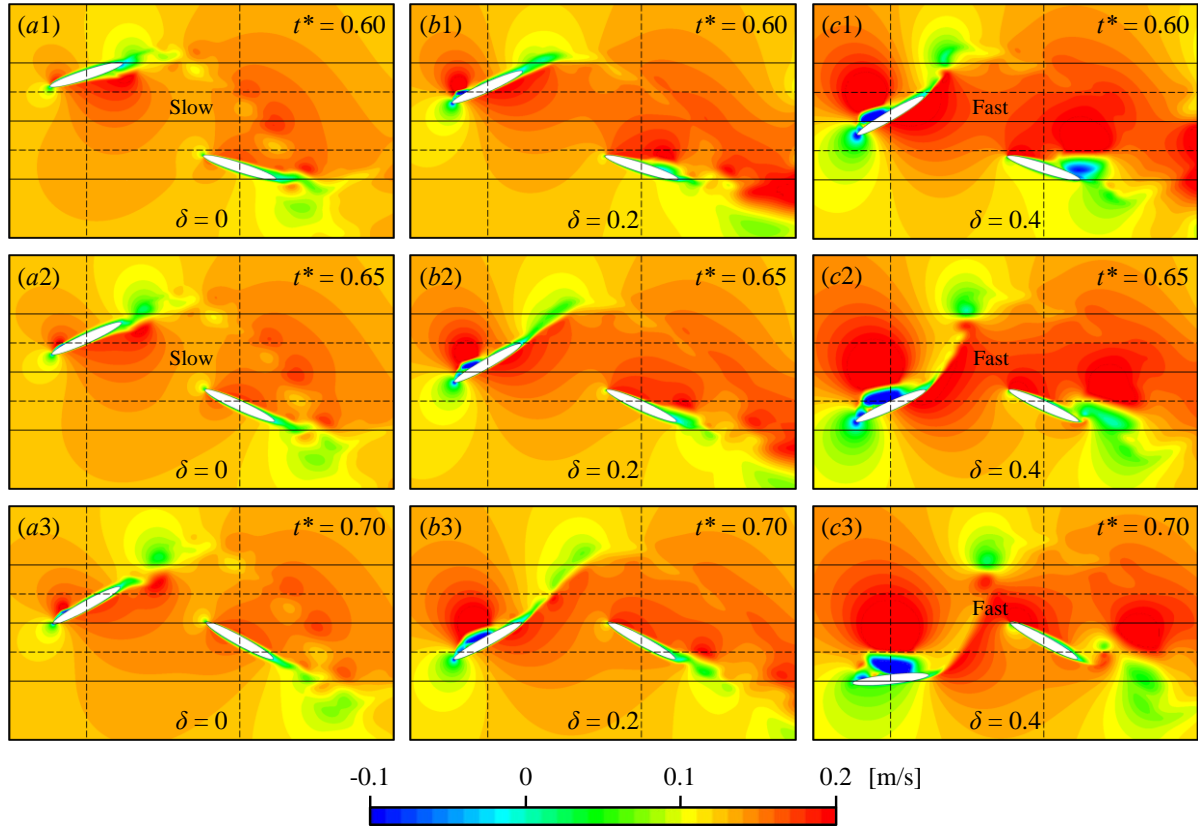


Figure 22. Instantaneous streamwise velocity fields of the tandem foils undergoing counterstroke flapping at various δ during the first half of a hindfoil upstroke: (a1) $t^* = 0.6$, $\delta = 0$; (a2) $t^* = 0.65$, $\delta = 0$; (a3) $t^* = 0.7$, $\delta = 0$; (b1) $t^* = 0.6$, $\delta = 0.2$; (b2) $t^* = 0.65$, $\delta = 0.2$; (b3) $t^* = 0.7$, $\delta = 0.2$; (c1) $t^* = 0.6$, $\delta = 0.4$; (c2) $t^* = 0.65$, $\delta = 0.4$; (c3) $t^* = 0.7$, $\delta = 0.4$.

During the second half of the upstroke, Figure 18(b) illustrates that the hindfoil gains a thrust peak with its magnitude increasing with δ , implying an enhancement in thrust production via asymmetric flapping. Conversely, the lift coefficient in Figure 18(d) is subjected to a significant trough and its magnitude decreases with δ . The mechanism of force production converts from freestream-dominant to flapping-dominant during this period as the flapping velocity of the hindfoil increases, thereby generating thrust and negative lift. Furthermore,

Figure 24 indicates that the hindfoil passes through the shed vortices of the forefoil, forming constructive foil-vortex interactions. Therefore, additional thrust and negative lift are produced via pressure drop on the foil lower surface due to wake capture. The vortex shedding from the forefoil becomes much more consistent and stronger at larger values of δ , which enhances the wake capture and force production.

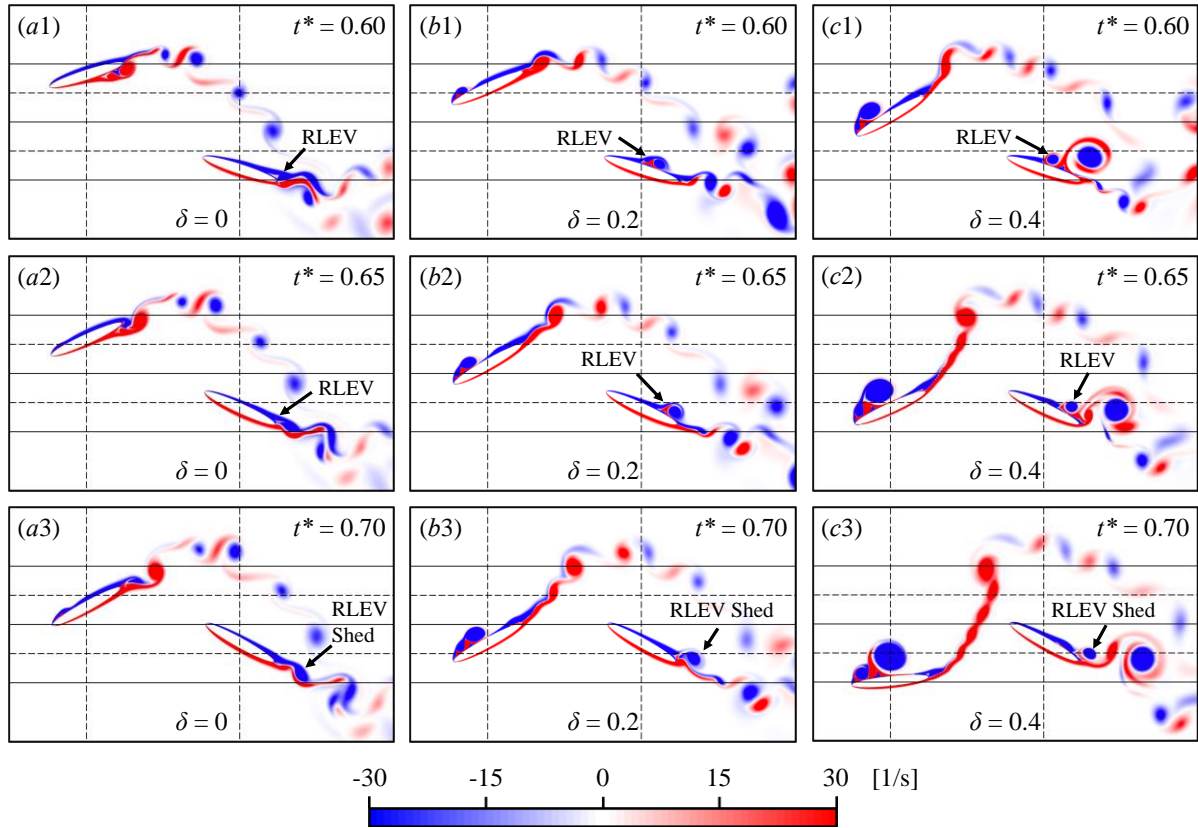


Figure 23. Instantaneous vorticity fields of the tandem foils undergoing counterstroke flapping at various δ during the first half of a hindfoil upstroke: (a1) $t^* = 0.6$, $\delta = 0$; (a2) $t^* = 0.65$, $\delta = 0$; (a3) $t^* = 0.7$, $\delta = 0$; (b1) $t^* = 0.6$, $\delta = 0.2$; (b2) $t^* = 0.65$, $\delta = 0.2$; (b3) $t^* = 0.7$, $\delta = 0.2$; (c1) $t^* = 0.6$, $\delta = 0.4$; (c2) $t^* = 0.65$, $\delta = 0.4$; (c3) $t^* = 0.7$, $\delta = 0.4$.

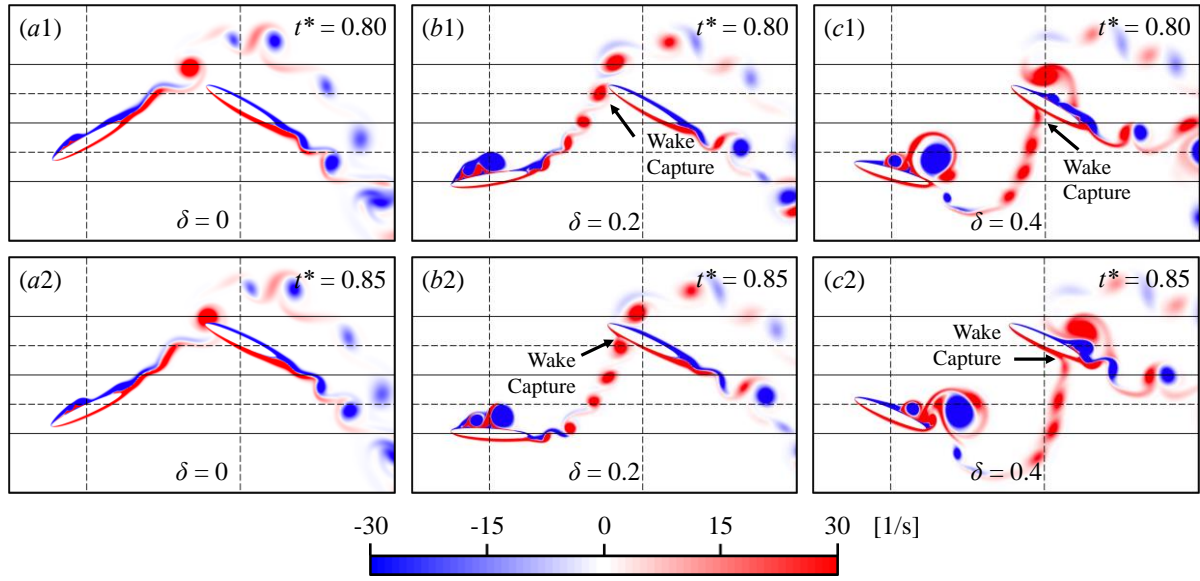


Figure 24. Instantaneous vorticity fields of the tandem foils undergoing counterstroke flapping at various δ during the second half of a hindfoil upstroke: (a1) $t^* = 0.8$, $\delta = 0$; (a2) $t^* = 0.85$, $\delta = 0$; (b1) $t^* = 0.8$, $\delta = 0.2$; (b2) $t^* = 0.85$, $\delta = 0.2$; (c1) $t^* = 0.8$, $\delta = 0.4$; (c2) $t^* = 0.85$, $\delta = 0.4$.

3.3.4 Summary of counterstroke flapping

It can be concluded that the thrust production on the forefoil is effectively enhanced during the downstroke but attenuated during the upstroke with the increase in δ , as illustrated in Figure 25(a). Moreover, the lift production is largely augmented throughout the whole stroke cycle. Such variations are associated with the change in flapping velocities between the up- and downstrokes.

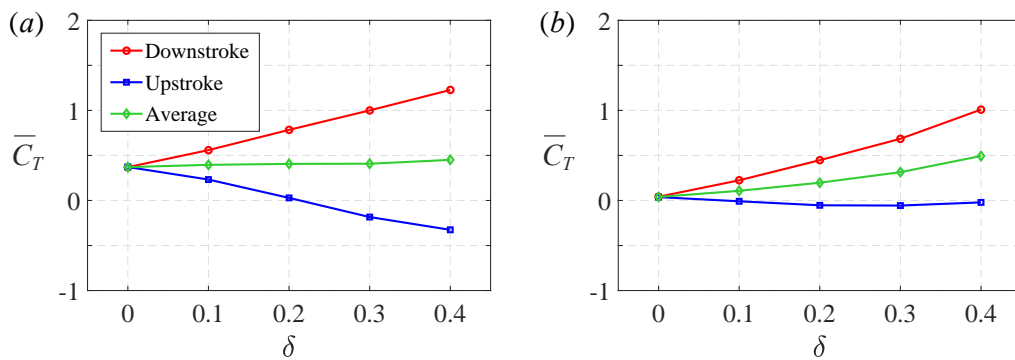


Figure 25. Mean thrust coefficients of the tandem foils at the up- and downstrokes, respectively: (a) the mean forefoil thrust coefficients; (b) the mean hindfoil thrust coefficients.

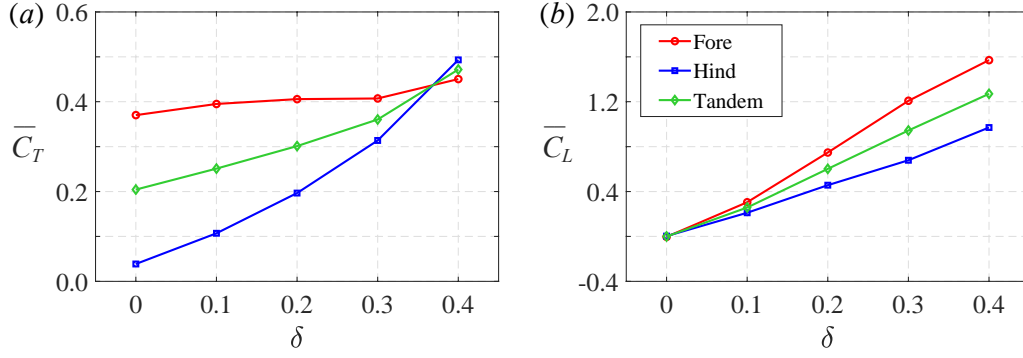


Figure 26. Mean thrust and lift coefficients of the tandem foils: (a) the mean thrust coefficients of the forefoil \bar{C}_{TF} , the hindfoil \bar{C}_{TH} , and the tandem-foil system \bar{C}_{TS} ; (b) the mean lift coefficients of the forefoil \bar{C}_{LF} , the hindfoil \bar{C}_{LH} , and the tandem-foil system \bar{C}_{LS} .

The downstroke performance of the hindfoil during time-asymmetric flapping is primarily governed by its flapping velocity, while the upstroke performance is associated with multiple aspects, including the flapping velocity, the wake capture, and the forefoil-induced flow velocity. When the hindfoil performs an accelerated downstroke, the forefoil should be in a decelerated upstroke, which can only generate limited interferences to the downstream. Therefore, the increased downstroke flapping velocity of the hindfoil becomes the primary factor that augments the force production. On the contrary, during the first half of the hindfoil upstroke, the thrust production is suppressed as the hindfoil flaps up much slower. The reduced flapping velocity coupled with the interferences from the forefoil and the RLEVs results in significant drag and positive lift. During the second half of the hindfoil upstroke, the foil-vortex interaction on the hindfoil is effectively reinforced with the increase in δ , as the vortex shedding by the forefoil becomes stronger and more consistent, thus augmenting the thrust production. Subsequently, the thrust loss of the hindfoil at the first half of the upstroke is compensated by the constructive foil-vortex interaction to a certain degree. This corresponds to the scenario that the mean upstroke thrust coefficient of the hindfoil does not reduce as δ increases in Figure 25(b).

Figure 26 summarizes the mean thrust and lift coefficients of the tandem-foil system against δ . Specifically, the thrust coefficient of the hindfoil significantly increases with δ and overcomes that of the forefoil at $\delta = 0.4$. By introducing the stroke time-asymmetry, the mean thrust coefficient of the tandem-foil system \bar{C}_{TS} improves by 2.5 times from 0.2 to almost 0.5 at $\delta = 0.4$ as illustrated in Figure 26(a). In terms of the lift coefficients, both foils demonstrate

considerable increases due to the change in flapping velocities between the up- and downstrokes. Subsequently, the mean lift coefficient of the tandem-foil system \bar{C}_{LS} surges from 0 to about 1.3 at $\delta = 0.4$.

3.4 Hindfoil-leading flapping ($\varphi = 90^\circ$)

In this section, the tandem foils are operated at a hindfoil-leading flapping mode where the hindfoil leads the forefoil by a phase difference of 90° . The instantaneous thrust coefficients of both foils at different δ are shown in Figure 27(a) and Figure 27(b), where the thrust production is enhanced during the downstroke but attenuated during the upstroke. The lift production of the two foils shown in Figure 27(c) and Figure 27(d) is generally augmented throughout the whole flapping cycle. These are likely due to the variation in flapping velocities between the up- and downstrokes, as explained in former subsections.

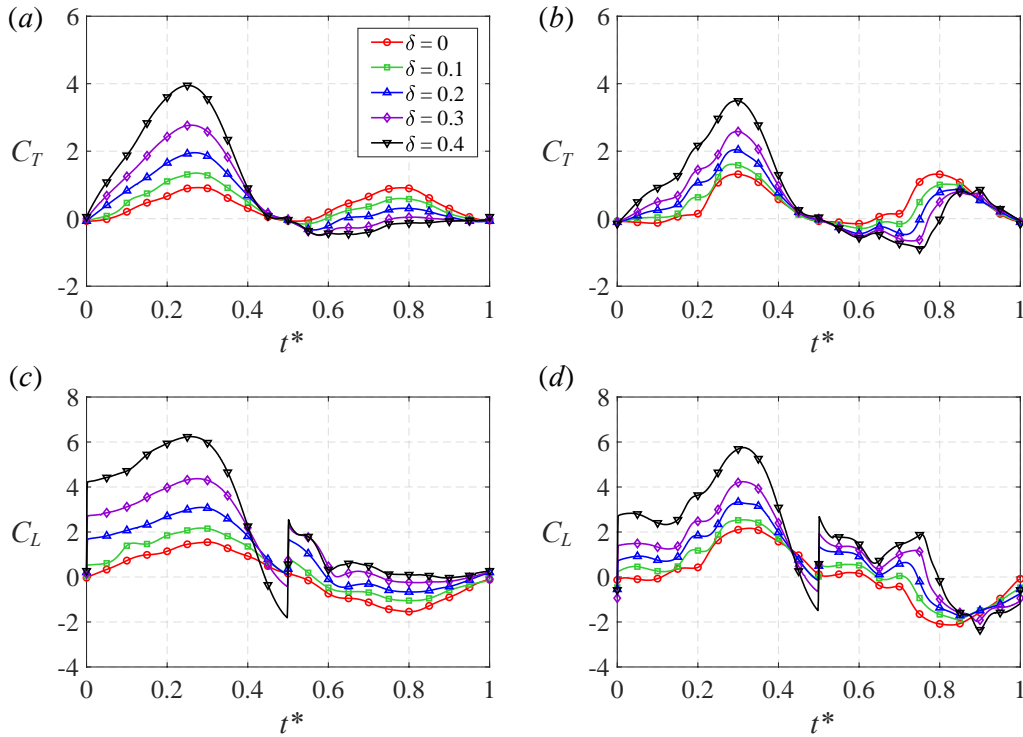


Figure 27. Instantaneous thrust and lift coefficients of the tandem foils undergoing hindfoil-leading flapping ($\varphi = 90^\circ$) at various δ : (a) the forefoil thrust coefficient, C_{TF} ; (b) the hindfoil thrust coefficient, C_{TH} ; (c) the forefoil lift coefficient, C_{LF} ; (d) the hindfoil lift coefficient, C_{LH} .

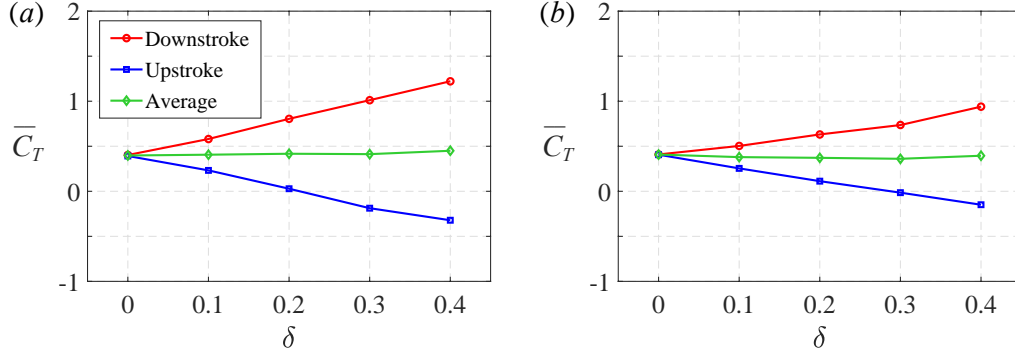


Figure 28. Mean thrust coefficients of the tandem foils at the up- and downstrokes, respectively: (a) the mean forefoil thrust coefficients; (b) the mean hindfoil thrust coefficients.

Figure 28 suggests that the mean thrust production is enhanced during the downstroke but weakened during the upstroke with the increase in δ , which is in accordance with the former two flapping modes. Regarding the overall performance of the tandem-foil system, Figure 29 illustrates that the mean thrust coefficient of the forefoil climbs modestly from 0.4 to 0.45 as δ increases from 0 to 0.4 while that of the hindfoil hovers between 0.35 and 0.4. Averaging across the fore- and hindfoils, the mean thrust coefficient of the tandem-foil system \bar{C}_{TS} approximately experiences a 5% increment as δ increases from 0 to 0.4. Meanwhile, the mean lift coefficient \bar{C}_{LS} surges from 0 to around 1.3, as shown in Figure 29(b), ascribing to the variation of flapping velocities between the up- and downstrokes.

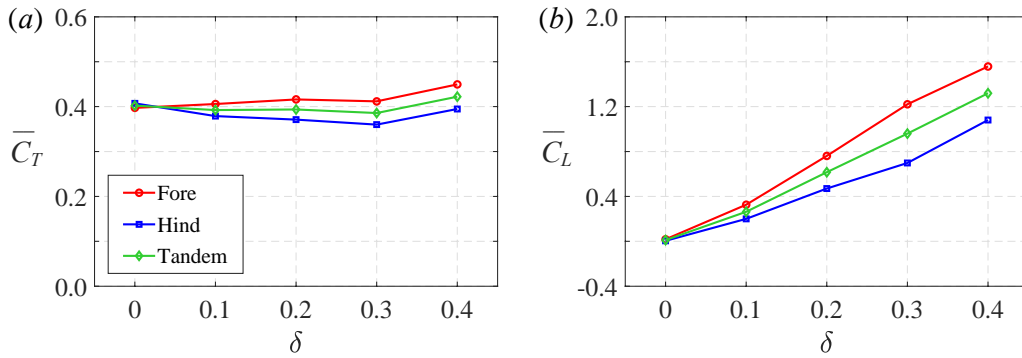


Figure 29. Mean thrust and lift coefficients of the tandem foils: (a) the mean thrust coefficients of the forefoil \bar{C}_{TF} , the hindfoil \bar{C}_{TH} , and the tandem-foil system \bar{C}_{TS} ; (b) the mean lift coefficients of the forefoil \bar{C}_{LF} , the hindfoil \bar{C}_{LH} , and the tandem-foil system \bar{C}_{LS} .

4. Conclusions

The effects of stroke time-asymmetry on the performances of tandem foils at a Reynolds number of 5000 are investigated using numerical and experimental methods. Different values

of the asymmetry ratio, ranging from 0 to 0.4, are considered at three different phase angles, in-phase ($\varphi = 0^\circ$), hindfoil-leading ($\varphi = 90^\circ$) and counterstroke ($\varphi = 180^\circ$). It is found that the foil performances can be enhanced by introducing time-asymmetric flapping kinematics with several key observations:

(1) For in-phase flapping, the mean thrust coefficient of the tandem-foil system increases by approximately 15% from 0.55 to 0.63 when δ increases from 0 to 0.4. Its magnitude remains the highest compared to the other two flapping modes, owing to the wake capture by the hindfoil.

(2) For counterstroke flapping, the mean thrust coefficient experiences a remarkable enhancement by 2.5 times from 0.2 to 0.5 as δ increases from 0 to 0.4. Such improvement benefits from the increased downstroke foil flapping velocities and the enhanced upstroke foil-vortex interactions at larger values of δ .

(3) For hindfoil-leading flapping, only a slight increment of 5% in thrust augmentation is achieved.

(4) The lift production is enhanced throughout the whole flapping cycle on both foils as the increased downstroke flapping velocities can augment the positive lift while the decreased upstroke velocities generate smaller negative lift. Besides, the enhancements in lift production via stroke time-asymmetry are found to be little affected by the change in phase relationships. When δ increases from 0 to 0.4, the lift coefficients at different phase angles surge up to between 1.3 and 1.5.

The study demonstrates that the force production on the forefoil is primarily affected by the variation in flapping velocities between the up- and downstrokes. Besides, the forefoil is insensitive to the change in phase relationships considering that the downstream effects on the upstream are insignificant for forward flight. In contrast, the hindfoil demonstrates much more complicated patterns as the force production is also varied by the foil-vortex interactions and the induced flow velocities by the forefoil according to the associated phase relationships. This study investigates the performance augmentation mechanism of tandem foils with stroke time-asymmetry, which can provide insights towards the design of efficient foil kinematics for high-performance biomimetic propulsors.

Acknowledgements

The authors would like to thank the Singapore Centre for 3D Printing, which is supported by the National Research Foundation, Prime Minister's Office, Singapore under its Medium-Sized Centre funding scheme, as well as the support from Nanyang Technological University through grant no. 04INS000329C160 and 04INS000453C160.

Appendix A. Supplementary material

Supplementary material related to this article can be found online.

References

- [1] D. Bie, D. Li, J. Xiang, H. Li, Z. Kan, Y. Sun, Design, aerodynamic analysis and test flight of a bat-inspired tailless flapping wing unmanned aerial vehicle, *Aerosp Sci Technol.* 112 (2021) 106557. <https://doi.org/10.1016/j.ast.2021.106557>.
- [2] X. Ke, W. Zhang, J. Shi, W. Chen, The modeling and numerical solution for flapping wing hovering wingbeat dynamics, *Aerosp Sci Technol.* 110 (2021) 106474. <https://doi.org/10.1016/j.ast.2020.106474>.
- [3] Z. Kamankesh, A. Banazadeh, Stability analysis for design improvement of bio-inspired flapping wings by energy method, *Aerosp Sci Technol.* 111 (2021) 106558. <https://doi.org/10.1016/j.ast.2021.106558>.
- [4] M.F. Platzer, K.D. Jones, J. Young, J.C.S. Lai, Flapping Wing Aerodynamics: Progress and Challenges, *Aiaa J.* 46 (2012) 2136–2149. <https://doi.org/10.2514/1.29263>.
- [5] Y. Lian, T. Broering, K. Hord, R. Prater, The characterization of tandem and corrugated wings, *Prog Aerosp Sci.* 65 (2014) 41–69. <https://doi.org/10.1016/j.paerosci.2013.08.001>.
- [6] J. Han, Z. Yuan, G. Chen, Effects of kinematic parameters on three-dimensional flapping wing at low Reynolds number, *Phys Fluids.* 30 (2018) 081901. <https://doi.org/10.1063/1.5041292>.
- [7] J. Wu, H. Yan, C. Zhou, Y. Zhang, Unsteady aerodynamics of a micro flapping rotary wing in forward flight, *Aerosp Sci Technol.* 111 (2021) 106530. <https://doi.org/10.1016/j.ast.2021.106530>.
- [8] Z.J. Wang, D. Russell, Effect of Forewing and Hindwing Interactions on Aerodynamic Forces and Power in Hovering Dragonfly Flight, *Phys Rev Lett.* 99 (2007) 148101. <https://doi.org/10.1103/physrevlett.99.148101>.
- [9] T. Broering, Y. Lian, W. Henshaw, Numerical Study of Two Flapping Airfoils in Tandem Configuration, 48th Aiaa Aerosp Sci Meet Incl New Horizons Forum Aerosp Expo. (2010). <https://doi.org/10.2514/6.2010-865>.
- [10] T.M. Broering, Y.-S. Lian, The effect of phase angle and wing spacing on tandem flapping wings, *Acta Mech Sinica.* 28 (2012) 1557–1571. <https://doi.org/10.1007/s10409-012-0210-8>.
- [11] T.M. Broering, Y. Lian, W. Henshaw, Numerical Investigation of Energy Extraction in a Tandem Flapping Wing Configuration, *Aiaa J.* 50 (2012) 2295–2307. <https://doi.org/10.2514/1.j051104>.
- [12] B.M. Boschitsch, P.A. Dewey, A.J. Smits, Propulsive performance of unsteady tandem hydrofoils in an in-line configuration, *Phys Fluids 1994-Present.* 26 (2014) 051901. <https://doi.org/10.1063/1.4872308>.

- [13] N. Gravish, J.M. Peters, S.A. Combes, R.J. Wood, Collective Flow Enhancement by Tandem Flapping Wings, *Phys Rev Lett.* 115 (2015) 188101. <https://doi.org/10.1103/physrevlett.115.188101>.
- [14] T.M. Broering, Y. Lian, Numerical study of tandem flapping wing aerodynamics in both two and three dimensions, *Comput Fluids.* 115 (2015) 124–139. <https://doi.org/10.1016/j.compfluid.2015.04.003>.
- [15] K.B. Lua, H. Lu, X.H. Zhang, T.T. Lim, K.S. Yeo, Aerodynamics of two-dimensional flapping wings in tandem configuration, *Phys Fluids.* 28 (2016) 121901. <https://doi.org/10.1063/1.4971859>.
- [16] L. Shilong, S. Mao, Aerodynamic force and flow structures of two airfoils in flapping motions, *Acta Mech Sinica.* 17 (2001) 310–331. <https://doi.org/10.1007/bf02487459>.
- [17] W.J. Maybury, F.-O. Lehmann, The fluid dynamics of flight control by kinematic phase lag variation between two robotic insect wings, *J Exp Biol.* 207 (2004) 4707–4726. <https://doi.org/10.1242/jeb.01319>.
- [18] M. Sun, S.L. Lan, A computational study of the aerodynamic forces and power requirements of dragonfly (*Aeschna juncea*) hovering, *J Exp Biol.* 207 (2004) 1887–1901. <https://doi.org/10.1242/jeb.00969>.
- [19] J.K. Wang, M. Sun, A computational study of the aerodynamics and forewing-hindwing interaction of a model dragonfly in forward flight, *J Exp Biol.* 208 (2005) 3785–3804. <https://doi.org/10.1242/jeb.01852>.
- [20] J.R. Usherwood, F.-O. Lehmann, Phasing of dragonfly wings can improve aerodynamic efficiency by removing swirl, *J Roy Soc Interface.* 5 (2008) 1303–1307. <https://doi.org/10.1098/rsif.2008.0124>.
- [21] D. Rival, D. Schönweitz, C. Tropea, Vortex interaction of tandem pitching and plunging plates: a two-dimensional model of hovering dragonfly-like flight., *Bioinspir Biomim.* 6 (2011) 016008. <https://doi.org/10.1088/1748-3182/6/1/016008>.
- [22] L.E. Muscutt, G.D. Weymouth, B. Ganapathisubramani, Performance augmentation mechanism of in-line tandem flapping foils, *J Fluid Mech.* 827 (2017) 484–505. <https://doi.org/10.1017/jfm.2017.457>.
- [23] N.S. Lagopoulos, G.D. Weymouth, B. Ganapathisubramani, Deflected wake interaction of tandem flapping foils, *J Fluid Mech.* 903 (2020) A9. <https://doi.org/10.1017/jfm.2020.640>.
- [24] Y. Zheng, Y. Wu, H. Tang, A time-resolved PIV study on the force dynamics of flexible tandem wings in hovering flight, *J Fluid Struct.* 62 (2016) 65–85. <https://doi.org/10.1016/j.jfluidstructs.2015.12.008>.
- [25] Y. Yu, B. Tong, A flow control mechanism in wing flapping with stroke asymmetry during insect forward flight, *Acta Mech Sinica.* 21 (2005) 218–227. <https://doi.org/10.1007/s10409-005-0032-z>.

- [26] F.M. Bos, D. Lentink, B.W.V. Oudheusden, H. BIJL, Influence of wing kinematics on aerodynamic performance in hovering insect flight, *J Fluid Mech.* 594 (2007) 341–368. <https://doi.org/10.1017/s0022112007009172>.
- [27] Q. Xiao, W. Liao, Numerical study of asymmetric effect on a pitching foil, *Int J Mod Phys C.* 20 (2009) 1663–1680. <https://doi.org/10.1142/s0129183109014667>.
- [28] K. Lu, Y.H. Xie, D. Zhang, Numerical study of large amplitude, nonsinusoidal motion and camber effects on pitching airfoil propulsion, *J Fluid Struct.* 36 (2013) 184–194. <https://doi.org/10.1016/j.jfluidstructs.2012.10.004>.
- [29] K. Lu, Y.H. Xie, D. Zhang, J.B. Lan, Numerical investigations into the asymmetric effects on the aerodynamic response of a pitching airfoil, *J Fluid Struct.* 39 (2013) 76–86. <https://doi.org/10.1016/j.jfluidstructs.2013.02.001>.
- [30] Z. Xingwei, Z. Chaoying, Numerical Investigation on the Aerodynamic Characteristics of a Forward Flight Flapping Airfoil with Nonsymmetrical Plunging Motion, *Information Technology J.* 10 (2011) 748–758. <https://doi.org/10.3923/itj.2011.748.758>.
- [31] J. Zhu, C. Zhou, Aerodynamic performance of a two-dimensional flapping wing in asymmetric stroke, *Proc Institution Mech Eng Part G J Aerosp Eng.* 228 (2012) 641–651. <https://doi.org/10.1177/0954410012474135>.
- [32] C. Wang, C. Zhou, P. Xie, Numerical investigation on aerodynamic performance of a 2-D inclined hovering wing in asymmetric strokes, *J Mech Sci Technol.* 30 (2016) 199–210. <https://doi.org/10.1007/s12206-015-1223-6>.
- [33] Y.-Y. Liu, C. Pan, Y. Zhou, Y. Liu, Visualization on vortical structures in the wake of a pair of pitching wings with asymmetrical motion, *J Visual-Japan.* 23 (2020) 185–190. <https://doi.org/10.1007/s12650-019-00616-y>.
- [34] P. Nian, B. Song, J. Xuan, W. Zhou, D. Xue, Study on flexible flapping wings with three dimensional asymmetric passive deformation in a flapping cycle, *Aerosp Sci Technol.* 104 (2020) 105944. <https://doi.org/10.1016/j.ast.2020.105944>.
- [35] S. Deng, J. Wang, H. Liu, Experimental study of a bio-inspired flapping wing MAV by means of force and PIV measurements, *Aerosp Sci Technol.* 94 (2019) 105382. <https://doi.org/10.1016/j.ast.2019.105382>.
- [36] G.K. Taylor, R.L. Nudds, A.L.R. Thomas, Flying and swimming animals cruise at a Strouhal number tuned for high power efficiency, *Nature.* 425 (2003) 707–711. <https://doi.org/10.1038/nature02000>.
- [37] K. Grayson, C.M. de Silva, N. Hutchins, I. Marusic, Impact of mismatched and misaligned laser light sheet profiles on PIV performance, *Exp Fluids.* 59 (2017) 2. <https://doi.org/10.1007/s00348-017-2453-4>.
- [38] W. Thielicke, E.J. Stamhuis, PIVlab – Towards User-friendly, Affordable and Accurate Digital Particle Image Velocimetry in MATLAB, *J Open Res Softw.* 2 (2014) e30. <https://doi.org/10.5334/jors.bl>.

[39] Z.J. Wang, Vortex shedding and frequency selection in flapping flight, *J Fluid Mech.* 410 (2000) 323–341. <https://doi.org/10.1017/s0022112099008071>.

[40] K.B. Lua, S.M. Dash, T.T. Lim, K.S. Yeo, On the thrust performance of a flapping two-dimensional elliptic airfoil in a forward flight, *J Fluid Struct.* 66 (2016) 91–109. <https://doi.org/10.1016/j.jfluidstructs.2016.07.012>.